INSTITUTE OF PHYSICS PUBLISHING REPORTS ON PROGRESS IN PHYSICS

Rep. Prog. Phys. **69** (2006) 507–561 doi:10.1088/0034-4885/69/3/R01

# Physics of carbon nanotube electronic devices

**M P Anantram**[1] **and F Léonard**[2]

[1] Center for Nanotechnology, NASA Ames Research Center, Mail Stop: 229-1, Moffett Field, CA 94035-1000, USA
[2] Nanoscale Science and Technology Department, Sandia National Laboratories, Livermore, CA 94551, USA

E-mail: anant@arc.nasa.gov and fleonar@sandia.gov

Received 6 September 2005, in final form 1 November 2005
Published 1 February 2006
Online at stacks.iop.org/RoPP/69/507

## Abstract

Carbon nanotubes (CNTs) are amongst the most explored one-dimensional nanostructures and have attracted tremendous interest from fundamental science and technological perspectives. Albeit topologically simple, they exhibit a rich variety of intriguing electronic properties, such as metallic and semiconducting behaviour. Furthermore, these structures are atomically precise, meaning that each carbon atom is still three-fold coordinated without any dangling bonds. CNTs have been used in many laboratories to build prototype nanodevices. These devices include metallic wires, field-effect transistors, electromechanical sensors and displays. They potentially form the basis of future all-carbon electronics.

This review deals with the building blocks of understanding the device physics of CNT-based nanodevices. There are many features that make CNTs different from traditional materials, including chirality-dependent electronic properties, the one-dimensional nature of electrostatic screening and the presence of several direct bandgaps. Understanding these novel properties and their impact on devices is crucial in the development and evolution of CNT applications.

(Some figures in this article are in colour only in the electronic version)

  

## Contents

## 1. Introduction

Due to their low dimensionality, nanostructures such as quantum dots, nanowires and carbon nanotubes (CNTs) possess unique properties that make them promising candidates for future technology applications. However, to truly harness the potential of nanostructures, it is essential to develop a fundamental understanding of the basic physics that governs their behaviour in devices. This is especially true for CNTs, where, as will be discussed in this review, research has shown that the concepts learned from bulk device physics do not simply carry over to nanotube devices, leading to unusual device operation. For example, the properties of bulk metal/semiconductor contacts are usually dominated by Fermi level pinning; in contrast, the quasi-one-dimensional structure of nanotubes leads to a much weaker effect of Fermi level pinning, allowing for tailoring of contacts by metal selection. Similarly, while strain effects in conventional silicon devices have been associated with mobility enhancements, strain in CNTs takes an entirely new perspective, with strain-induced bandgap and conductivity changes.

CNTs also present a unique opportunity as one of the few systems where atomistic-based modelling may reach the experimental device size, thus in principle allowing the experimental testing of computational approaches and computational device design. While similar approaches are under development for nanoscale silicon devices, the much different properties of CNTs require an entirely separate field of research.

This review presents recent experimental and theoretical work that has highlighted the new physics of CNT devices. Our review begins in this section with an introduction to the atomic and electronic structure of CNTs, establishing the basic concepts that will be useful in later sections. Section 2 discusses the properties of metallic CNTs for carrying electronic current, where potential applications include interconnects. Concepts of quantum conductance, quantum capacitance and quantum inductance are introduced as well as a discussion of the role of phonon and defect scattering. Section 3 addresses the important issue of contacts between metals and CNTs, focusing on the role of Fermi-level pinning, properties of contacts in CNT transistors and development of ultrathin oxides for contact insulation. The discussion in section 4 focuses on electronic devices with semiconducting CNTs as the active elements. The simplest such device, the p–n junction, is extensively discussed as an excellent example to illustrate the differences between CNTs and traditional devices. This discussion is followed by an exposé on metal/semiconductor rectifiers where both the metal and the semiconductor are CNTs. A significant part of this section is devoted to CNT transistors and to the recent scientific progress aimed at understanding their basic modes of operation. Section 5 discusses electromechanical devices and examines the progress in nanoelectromechanical devices, such as actuators and resonators, and strain effects on the electronic structure and conductance. The subject of displays is addressed in section 6 and the emerging area of optoelectronics with CNTs is discussed in section 7, reviewing the aspects of photoconductivity and electroluminescence. An outlook is presented in section 8.

### *1.1. Structure of CNTs*

To understand the atomic structure of CNTs, one can imagine taking the structure of graphite, as shown in figure 1, and removing one of the two-dimensional planes, which is called a graphene sheet. A single graphene sheet is shown in figure 2(*a*). A CNT can be viewed as a rolled-up graphene strip which forms a closed cylinder as shown in figure 2. The basis vectors $\boldsymbol{a}_1 = a(\sqrt{3}, 0)$ and $\boldsymbol{a}_2 = a(\sqrt{3}/2, 3/2)$ generate the graphene lattice, where $a = 0.142$ nm is the carbon–carbon bond length. A and B are the two atoms in the unit cell of graphene. In cutting the rectangular strip, one defines a circumferential vector, $\boldsymbol{C} = n\boldsymbol{a}_1 + m\boldsymbol{a}_2$, from which

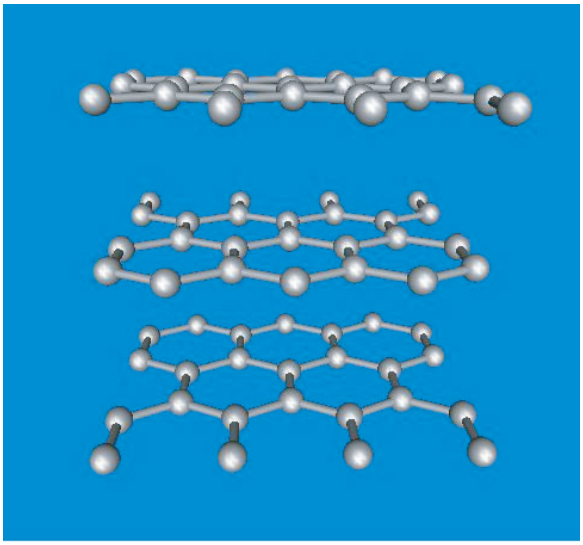

**Figure 1.** Illustration of the graphite structure, showing the parallel stacking of two-dimensional planes, called graphene sheets.

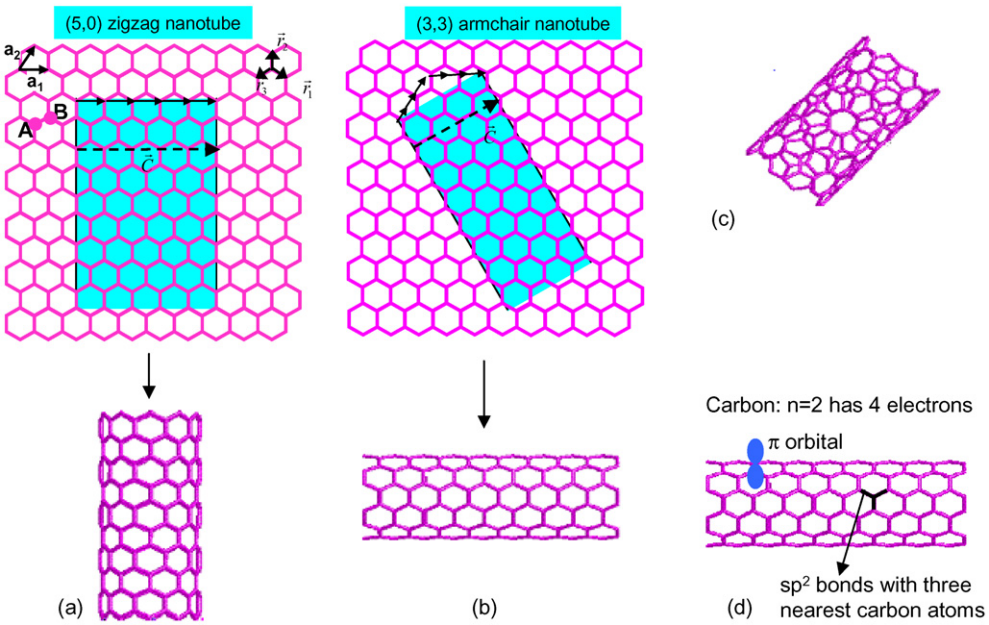


**Figure 2.** (*a*) $a_1$ and $a_2$ are the lattice vectors of graphene. $|\boldsymbol{a}_1| = |\boldsymbol{a}_2| = \sqrt{3}a$, where $a$ is the carbon–carbon bond length. There are two atoms per unit cell shown by A and B. SWNTs are equivalent to cutting a strip in the graphene sheet (blue) and rolling them up such that each carbon atoms is bonded to its three nearest neighbours. The creation of a $(n, 0)$ zigzag nanotube is shown. (*b*) Creation of a $(n, n)$ armchair nanotube. (*c*) A $(n, m)$ chiral nanotube. (*d*) The bonding structure of a nanotube. The $n = 2$ quantum number of carbon has four electrons. Three of these electrons are bonded to its three nearest neighbours by $sp^2$ bonding, in a manner similar to graphene. The fourth electron is a $\pi$ orbital perpendicular to the cylindrical surface.

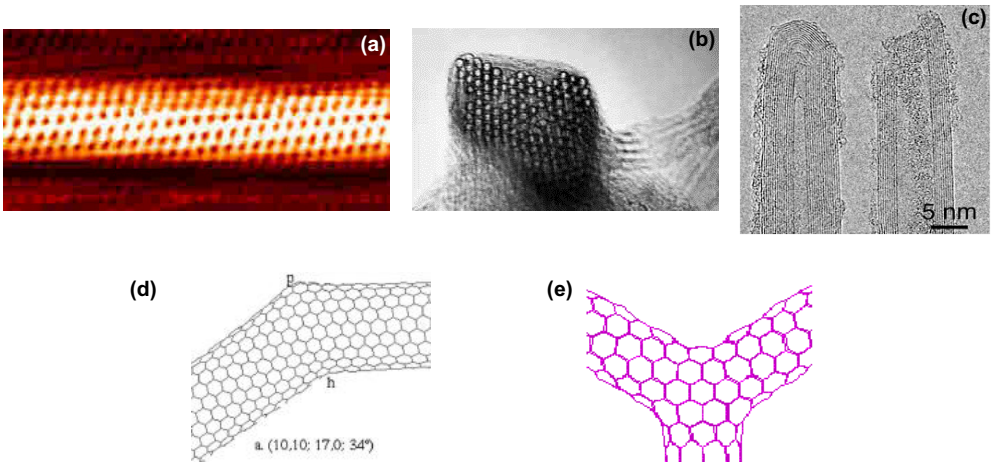


**Figure 3.** Forms of nanotubes: (*a*) STM image of a SWNT, (*b*) a bundle of SWNTs, (*c*) two MWNTs, (*d*) precise junction between two nanotubes of different chiralities and (*e*) three-terminal junction between nanotubes. In (*d*) and (*e*), each carbon atom has only three nearest neighbours and there are no dangling bonds. Figure sources (*a*) courtesy of C Dekker, (*b*) from [The96], (*c*) from [Bon99], (*d*) from [Han98], (*e*) courtesy of J Han.

the CNT radius can be obtained: $R = C/2\pi = (\sqrt{3}/2\pi)a\sqrt{n^2 + m^2 + nm}$. There are two special cases shown in figure 2 that deserve special mention. First, when the circumferential vector lies purely along one of the two basis vectors, the CNT is said to be of the 'zigzag' type. The example in figure 2(*a*) shows the generation of a (5,0) zigzag nanotube. Second, when the circumferential vector is along the direction exactly between the two basis vectors ($n = m$), the CNT is said to be of 'armchair' type. The example in figure 2(*b*) shows the generation of a (3,3) armchair nanotube. Figure 2(*c*) shows a nanotube with arbitrary chirality ($n, m$), where the blue strip is generated by $m \neq n$.

In a planar graphene sheet, the bonds to the three nearest neighbours of a carbon atom, $r_1$, $r_2$ and $r_3$ (figure 2(*a*)), are symmetrically placed. Rolling up a graphene sheet however causes differences in the three bonds. In the case of zigzag (armchair) nanotubes while the bonds oriented at a non-zero angle to the axis of the cylinder are identical, they are different from the axially (circumferentially) oriented bonds. All three bonds are slightly different for other chiral nanotubes.

We discussed the single wall nanotube (SWNT), which consists of a single layer of graphene strip. Nanotubes, however, are found in other closely related forms and shapes as shown in figure 3. Figure 3(*b*) shows a bundle of SWNTs with the CNTs arranged in a triangular lattice. The individual tubes in the bundle are attracted to their nearest neighbours via the van der Waals interactions, with typical distances between the tubes being comparable to the interplanar distance of graphite which is 3.1 Å. The cross section of an individual nanotube in a bundle is circular if the diameter is smaller than 15 Å and deforms to a hexagon as the diameter of the individual tubes increases [Ter94]. A close allotrope of the SWNT is the multiwall nanotube (MWNT), which consists of nested SWNTs, in a Russian doll fashion as shown in figure 3(*c*). Again, the distance between the walls of neighbouring tubes is comparable to the interplanar distance of graphite. CNTs also occur in more interesting shapes such as junctions between nanotubes of two different chiralities (figure 3(*d*)) and three terminal junctions (figure 3(*e*)). These CNT junctions are atomically precise in that each carbon atom is bonded primarily to its three nearest neighbours and there are no dangling bonds. The

curvature needed to create these interesting shapes arises from pentagon–heptagon defects in the hexagonal network.

### *1.2. Electronic properties of CNTs*

Each carbon atom in the hexagonal lattice described in section 1.1 possesses six electrons, and in the graphite structure carbon has two 1s electrons, three $2sp^2$ electrons and one 2p electron. The three $2sp^2$ electrons form the three bonds in the plane of the graphene sheet, leaving an unsaturated $\pi$ orbital (figure 2(*d*)). This $\pi$ orbital, perpendicular to the graphene sheet and thus the nanotube surface, forms a delocalized $\pi$ network across the nanotube, responsible for its electronic properties.

A carbon atom at position $\boldsymbol{r}_s$ has an unsaturated p orbital described by the wave function $\chi_{\boldsymbol{r}_s}(\boldsymbol{r})$. In the tight-binding representation, the interaction between orbitals on different atoms vanishes unless the atoms are nearest neighbours. Mathematically, this can be written as

$$\begin{aligned}&\langle\chi_{\boldsymbol{r}_A}|H|\chi_{\boldsymbol{r}_A}\rangle = \langle\chi_{\boldsymbol{r}_B}|H|\chi_{\boldsymbol{r}_B}\rangle = 0,\\ &\langle\chi_{\boldsymbol{r}_A}|H|\chi_{\boldsymbol{r}_B}\rangle = \langle\chi_{\boldsymbol{r}_B}|H|\chi_{\boldsymbol{r}_A}\rangle = \gamma\delta_{\boldsymbol{r}_A-\boldsymbol{r}_B=\boldsymbol{a}},\end{aligned} \tag{1.1}$$

where $a$ is a vector connecting nearest-neighbours between the A and B sublattices, and where we have set the on-site interaction energy to zero, without loss of generality. The A and B sublattices correspond to the set of all A and B atoms in figure 2(*a*), respectively.

To calculate the electronic structure, we construct the Bloch wavefunction for each of the sublattices as

$$\phi_{s\boldsymbol{k}}(\boldsymbol{r}) = \sum_{\boldsymbol{r}_s} \mathrm{e}^{\mathrm{i}\boldsymbol{k}\cdot\boldsymbol{r}_s}\chi_{\boldsymbol{r}_s}(\boldsymbol{r}), \tag{1.2}$$

where $s$ = A or B refers to each sublattice and $\boldsymbol{r}_s$ refers to the set of points belonging to sublattice $s$. The total wavefunction is then a linear combination of these two functions,

$$\psi_{\boldsymbol{k}}(\boldsymbol{r}) = \frac{1}{\sqrt{2}}[\phi_{A\boldsymbol{k}}(\boldsymbol{r}) + \lambda_{\boldsymbol{k}}\phi_{B\boldsymbol{k}}(\boldsymbol{r})]. \tag{1.3}$$

The Hamiltonian matrix elements are

$$\begin{aligned}&\langle\phi_{Ak}|H|\phi_{Ak}\rangle = \langle\phi_{Bk}|H|\phi_{Bk}\rangle = 0,\\ &\langle\phi_{Ak}|H|\phi_{Bk}\rangle = \langle\phi_{Bk}|H|\phi_{Ak}\rangle^* = H_{AB} = \gamma\sum_a \mathrm{e}^{\mathrm{i}\boldsymbol{k}\cdot\boldsymbol{a}},\end{aligned} \tag{1.4}$$

which leads to the Schrodinger equation in matrix form:

$$\begin{pmatrix} E & -H_{AB} \\ -H_{AB}^* & E \end{pmatrix}\begin{pmatrix} 1 \\ \lambda_k \end{pmatrix}. \tag{1.5}$$

Diagonalization of this matrix leads to the solution

$$E = \pm|H_{AB}| = \pm\gamma\sqrt{1 + 4\cos\left(\frac{3}{2}k_y a\right)\cos\left(\frac{\sqrt{3}}{2}k_x a\right) + 4\cos^2\left(\frac{\sqrt{3}}{2}k_x a\right)}. \tag{1.6}$$

This bandstructure for graphene is plotted in figure 4 as a function of $k_x$ and $k_y$. The valence and conduction bands meet at six points $[(\pm 4\pi/3\sqrt{3}a, 0); (\pm 2\pi/3\sqrt{3}a, \pm 2\pi/3a)]$ at the corner of the Brillouin zone. Graphene is thus described as a semi-metal: it has a non-zero density of states at the Fermi level, but the Fermi surface consists only of points.

To obtain the electronic structure of CNTs, we start from the bandstructure of graphene and quantize the wavevector in the circumferential direction:

$$k \cdot C = k_x C_x + k_y C_y = 2\pi p, \tag{1.7}$$

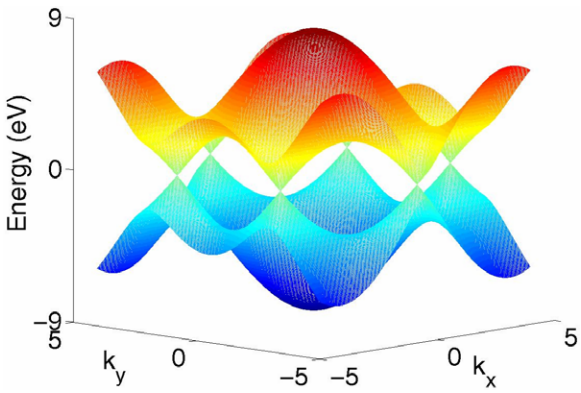


**Figure 4.** Electronic structure of graphene calculated within a tight-binding model consisting only of $\pi$ electrons.

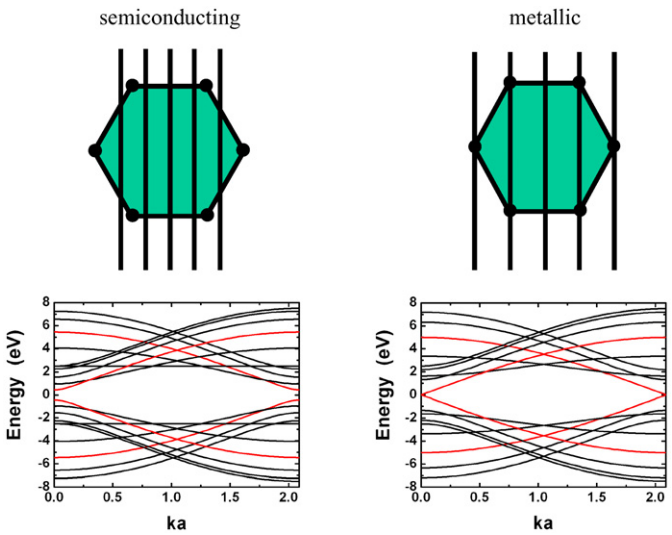


**Figure 5.** Illustration of allowed wavevector lines leading to semiconducting and metallic CNTs and examples of bandstructures for semiconducting and metallic zigzag CNTs.

where $\boldsymbol{C}$ is shown in figure 2 and $p$ is an integer. Equation (1.7) provides a relation between $k_x$ and $k_y$ defining lines in the $(k_x, k_y)$ plane. Each line gives a one-dimensional energy band by slicing the two-dimensional bandstructure of graphene shown in figure 4. The particular values of $C_x, C_y$ and $p$ determine where the lines intersect the graphene bandstructure, and thus each CNT will have a different electronic structure. Perhaps the most important aspect of this construction is that CNTs can be metallic or semiconducting, depending on whether or not the lines pass through the graphene Fermi points. This concept is illustrated in figure 5. In the left panels, the lines of quantized wavevectors do not intersect the graphene Fermi points and the CNT is semiconducting, with a bandgap determined by the two lines that come closer to the Fermi points. The right panel illustrates a situation where the lines pass through the Fermi points, leading to crossing bands at the CNT Fermi level and thus to a metallic character.

We can express mathematically the bandstructure of CNTs by defining components of the wavevector perpendicular and parallel to the tube axis. By expressing $k_x$ and $k_y$ in terms of

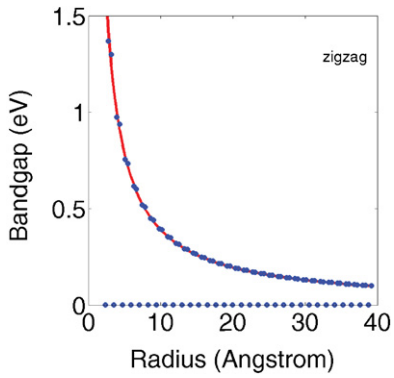


**Figure 6.** Bandgap versus radius for zigzag CNTs. The bandgap decreases inversely with increase in diameter. The points with zero bandgap correspond to metallic nanotubes which satisfy $n - m = 3 * I$, where $I$ is an integer. Note that when curvature induced effects are introduced all metallic nanotubes (except armchair) develop a small bandgap.

these components and substituting in (1.6), we obtain

$$E(k) = \pm\gamma \left[ 1 + 4\cos\left(\frac{3C_x ka}{2C} - \frac{3\pi paC_y}{C^2}\right)\cos\left(\frac{\sqrt{3}C_y ka}{2C} + \frac{\sqrt{3}\pi paC_x}{C^2}\right) + 4\cos^2\left(\frac{\sqrt{3}C_y ka}{2C} + \frac{\sqrt{3}\pi paC_x}{C^2}\right)\right]^{1/2}, \tag{1.8}$$

where $k$ is the wavevector in the axial direction, $C_x = a(\sqrt{3}n + (\sqrt{3}/2)m)$ and $C_y = a(3/2)m$. Bandstructures for semiconducting and metallic CNTs computed from this expression are shown in figure 5.

As discussed above, the condition for CNTs to be metallic is that some of the allowed lines $(2\pi p/C_y) - (C_x/C_y)k_x$ cross one of the Fermi points of graphene. This leads to the condition $|n - m| = 3 * I$ where $I$ is an integer. Nanotubes for which this condition does not hold are semiconducting. Furthermore, it can be shown that the bandgap of semiconducting nanotubes decreases inversely with an increase in diameter as shown in figure 6. The relationship between the bandgap and diameter [Whi93, Whi05] can be obtained by finding the two lines that come closest to a graphene Fermi point, giving a bandgap, $E_g \sim \gamma a/R$, as shown in figure 6.

The above model is also useful to understand the unusual density of states of CNTs. The density of states can be expressed as

$$D(E) = \frac{\sqrt{3}a^2}{2\pi R}\sum_i \int \mathrm{d}k\,\delta(k - k_i)\left|\frac{\partial\varepsilon}{\partial k}\right|^{-1}, \tag{1.9}$$

where $\varepsilon(k_i) = E$. Figure 7 shows the DOS calculated from (1.8) and (1.9) for (11,0) and (12,0) nanotubes. The unique feature here is the presence of singularities at the band edges. To understand the basic features of the DOS, one can expand the dispersion relation (1.6) around the Fermi point. This gives [Min98]

$$D(E) = \frac{a\sqrt{3}}{\pi^2 R\gamma}\sum_{m=1}^{N}\frac{|E|}{\sqrt{E^2 - \varepsilon_m^2}}, \tag{2.0}$$

where $\varepsilon_m = |3m + 1|(a\gamma/2R)$ for semiconducting tubes and $\varepsilon_m = |3m|(a\gamma/2R)$ for metallic tubes. In the case of metallic tubes, the $m = 0$ band gives a non-zero density of states at the

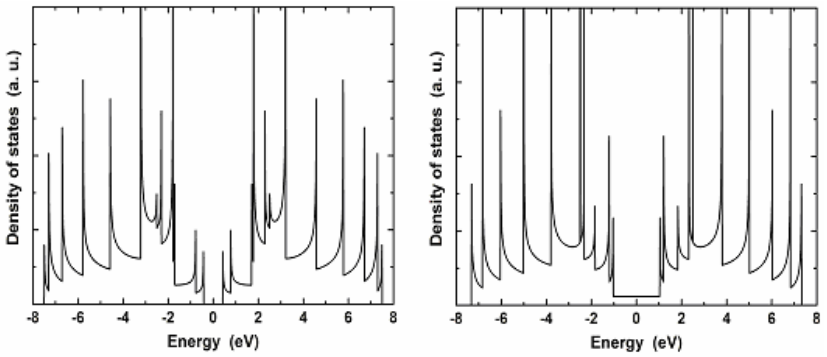


**Figure 7.** Density of states for (11,0) and (12,0) CNTs computed from tight binding show van Hove singularities.

Fermi level, with $D(E) = (a\sqrt{3})/(\pi^2 R\gamma)$. The expression for the density of states shows van Hove singularities when $E = \pm\varepsilon_m$, which is indicative of quasi-one-dimensional materials (figure 7). The presence of these singularities in the density of states has been verified by scanning-tunnelling microscopy of individual nanotubes [Wil98].

Finally, it is important to note that there are some deviations in the electronic properties of nanotubes from the simple $\pi$-orbital graphene picture described above, due to curvature. As a result of curvature (i) the hopping integrals describing the three bonds between nearest neighbours are not identical and (ii) $\sigma$–$\pi$ hybridization and charge self-consistency become important. Since curvature becomes larger with a decrease in the nanotube diameter, deviations from the simple $\pi$-orbital graphene picture become more important in small diameter nanotubes. Nanotubes satisfying $n - m = 3 * I$ develop a small curvature-induced bandgap and are hence semi-metallic. Armchair nanotubes are an exception because of their special symmetry, and they remain metallic for all diameters. The bandgap of semi-metallic nanotubes is small and varies inversely as the square of nanotube diameter. For example, while a semiconducting nanotube with a diameter of 10 Å has a bandgap of 1 eV, a semi-metallic nanotube with a comparable diameter has a bandgap of only 40 meV.

In graphene, hybridization between $\sigma$ and $\pi$ orbitals is absent. In contrast, the curvature of a nanotube induces $\sigma$–$\pi$ hybridization and the resulting changes in long-range interactions. While the influence of $\sigma$–$\pi$ hybridization in affecting the electronic properties of large diameter nanotubes is negligible, small diameter nanotubes are significantly affected. [Cab03] found that while tight-binding calculations predict small diameter (4,0) and (5,0) zigzag nanotubes to be semiconducting with bandgaps exceeding 1 eV, DFT–LDA calculations show that they are semi-metallic. Similarly, while tight-binding calculations predict the (6,0) zigzag nanotube to be semi-metallic with a bandgap of approximately 200 meV, DFT–LDA calculations indicate that they are metallic [Bla94, Cab03]. Overall, small diameter nanotubes require a more careful treatment beyond the simple tight-binding graphene model.

## 2. Metallic CNTs

### *2.1. Introduction*

Metallic CNTs have attracted significant attention because their current carrying ability is unparalleled in the family of emerging nanowires. Ballistic transport has been observed and

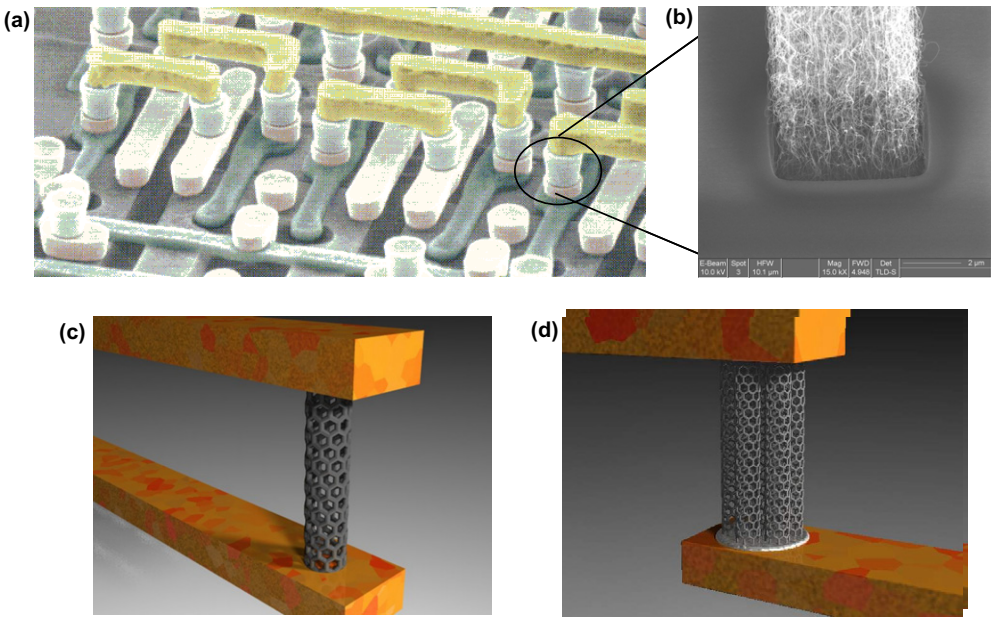


**Figure 8.** (*a*) A pictorial representation of the wiring in an integrated circuit. The horizontal interconnects are shown in yellow and the vertical interconnects are shown in grey. (*b*) An example of a MWNT array grown in a silicon oxide via, which can potentially be used as a vertical interconnect provided excellent electrical contacts can be made to both the top and bottom of the nanotube array. (*c*) A pictorial representation of the limit where a SWNT is used as a vertical interconnect in what may eventually become a molecular circuit. (*d*) An interconnect based on a bundle of SWNTs will have a low bias resistance of 6.5 kΩ divided by the number of nanotubes. (Source: (*a*) IBM Journal of Research and Development, (*b*) from [Kre02], (*c*) and (*d*) courtesy of Infineon Technologies.)

values for the conductance that approaches the theoretical limit have been measured at small biases. They hold promise as interconnects in both silicon nanoelectronics and molecular electronics because of their low resistance and strong mechanical properties (figure 8). An emerging problem with interconnects in the silicon industry is the breakdown of copper wires due to electromigration when current densities exceed $10^6$ A cm$^{-2}$. Preliminary work has shown that an array of nanotubes can be integrated with silicon technology and holds promise as vertical vias to carry more than an order of magnitude larger current densities than conventional vias [Kre02, Ngo04]. [Wei01] demonstrated that MWNTs carry current densities approaching $10^9$ A cm$^{-2}$. Single wall metallic nanotubes, with diameters as small as 5 Å, are also important from the perspective of molecular electronics, where they can be used as either interconnects or nanoscale contacts.

The unique bandstructure of metallic CNTs, which is partly responsible for their superb current carrying capacity deviates significantly from the parabolic bandstructure of a free electron in a nanowire (within the effective mass approximation). We will now discuss essential aspects of the nanotube bandstructure that are necessary to understand their current–voltage characteristics. The bandstructure and transmission versus the electron energy of a single wall armchair metallic nanotube is shown in figure 9. The bandstructure shows various subbands arising from quantization of the wave vector around the circumference of the nanotube. The transmission changes by an integer when a subband opens or closes. The magnitude of transmission change corresponds to the subband degeneracy. For example, the subbands shown

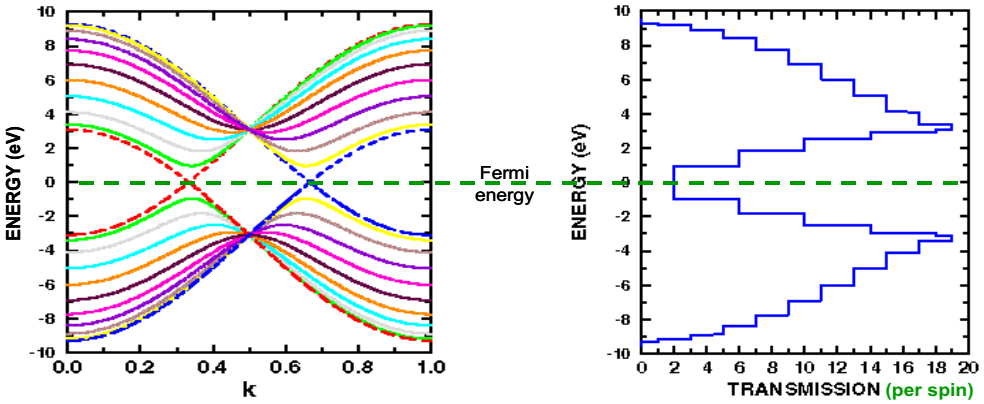


**Figure 9.** Left: energy versus wave vector ($k$) for a (10,10) armchair metallic nanotube. Right: energy versus total transmission per spin degree of freedom for the (10,10) nanotube.

by the dashed lines passing through the zero of energy are single-fold degenerate. Hence, the total transmission at the zero of energy is two units of quantum conductance. At about 0.85 eV, the transmission jumps from two to six units because the subbands shown in green and yellow colours are two-fold degenerate.

The number of subbands increases with an increase in the nanotube diameter because of an increase in the total number of quantum numbers arising from quantization of the electron wave function around the nanotube circumference. The general features of metallic CNTs are given as follows.

- Because the conductance and valence bands have mirror symmetry, the Fermi energy is at the energy where the subbands denoted by the dashed lines cross (which occurs at zero of energy in figure 9), independent of nanotube diameter. The location of the wave vector ($k$), where this crossing point occurs changes with nanotube chirality. These subbands are called crossing subbands.
- There are only two subbands per spin at the Fermi energy, independent of nanotube diameter and chirality.
- The energy of the first semiconducting subbands (first set of solid lines above and below zero of energy in figure 9) from the Fermi energy decreases inversely with the increase in nanotube diameter. For a nanotube with a diameter of about 15 (180) Å, the first semiconducting subband opens 0.85 (0.0625) eV away from the Fermi energy. Note that the semiconducting subbands are also referred to as non-crossing subbands.

From a basic physics perspective, metallic nanotubes have been of immense interest to researchers studying electron–electron interactions in condensed matter systems because they exhibit the novel physics of Luttinger liquid behaviour. We will however restrict ourselves to properties of nanotubes that emerge from their single particle physics in this review and refer the interested reader to [Boc99a, Gra01, Tar01] to learn about their Luttinger liquid properties. In the rest of this section, we will discuss the physics dictating the current-carrying properties of metallic nanotubes in low and high bias regimes in sections 2.2 and 2.3, respectively, and discuss the quantum capacitance, kinetic inductance and speed of signal propagation in section 2.4.

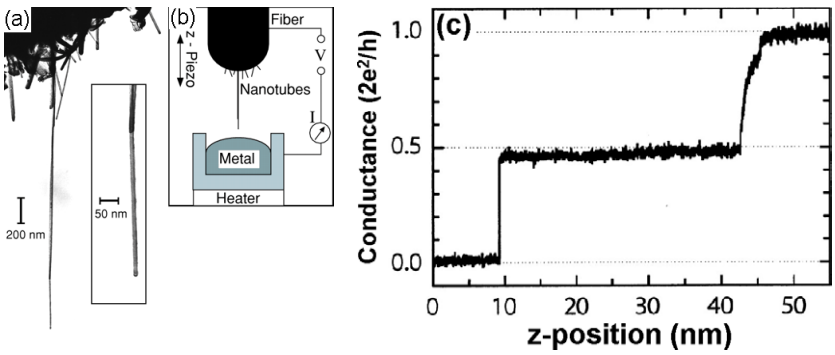


**Figure 10.** (*a*) Transmission electron micrograph of the end of a nanotube fibre recovered from the nanotube arc deposit. The long nanotube is 2.2 $\mu$m long and 14 nm wide. The inset shows the end of the longest tube under higher magnification; it is bundled together with another one that terminates 400 nm before the first one. (*b*) Schematic diagram of the experimental set-up. The nanotube contact is lowered under SPM control to a liquid metal surface. After contact is established, the current $I$ is measured as the fibre is moved into the liquid metal, so that the conductance can be determined as a function of the position of the nanotube contact. (*c*) Conductance as a function of dipping length into liquid mercury contact. The quantized conductance of $2e^2/h$ corresponds to a single nanotube making contact with mercury. The other quantized conductance values correspond to two and three nanotubes making contact with metal. From [Fra98].

### *2.2. Low bias transport*

The linear response conductance is given by

$$G = \frac{2e^2}{h} \sum_m \int \mathrm{d}E T_m(E) \left( -\frac{\partial f(E)}{\partial E} \right), \tag{2.2.1}$$

where the summation is over all modes $m$ and $f(E)$ is the Fermi–Dirac function. The term $\partial f/\partial E$ is significant only at energies near the Fermi energy; noting that the number of subbands at the Fermi energy is two, the linear response conductance is

$$G = \frac{2e^2}{h} \times \text{number of modes at Fermi energy} = \frac{4e^2}{h} = \frac{1}{6.5\ \mathrm{k}\Omega} \tag{2.2.2}$$

We have explicitly assumed that the nanotube diameter is small enough so that $\partial f/\partial E$ is negligible at energies corresponding to the semiconducting subbands. Experiments have measured small bias conductances between $2e^2/h$ and $4e^2/h$. A classic experiment that measured the small bias conductance of MWNTs involved two unconventional contacts, an SPM tip and liquid metal [Fra98]. The experimental set-up is shown in figure 10. The liquid metals used were mercury, cerrolow and gallium. In all the cases, the small bias conductance is $2e^2/h$, which is half the maximum possible value (equation (2.2.2)) for a single nanotube. The conductance increased in steps of $2e^2/h$ with the increase in the number of nanotubes making contact with the liquid metal. Modelling of this experimental effect has been challenging and a clear explanation is pending. [San00] found that inter-wall interactions modified the density of states near the Fermi level so as to decrease the conductance to $2e^2/h$. On the other hand, modelling of metal-armchair nanotube contacts using a jellium model shows that only one of the modes at the Fermi energy couples to the metal; the other mode does not couple well to the metal due to the wave vector mismatch [Ana00b] or reflection at the nanotube–metal interface [Cho99]. In contrast to armchair nanotubes, both subbands of zigzag nanotubes couple well to a jellium metal and hence are capable of carrying twice as much current, close

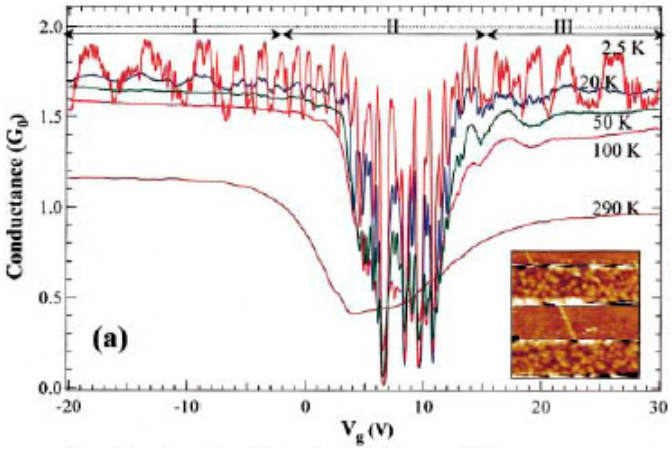


**Figure 11.** Conductance versus gate voltage for a metallic SWNT. The inset shows the nanotube lying between four metal contacts. As the temperature is lowered, the conductance approaches $2G_0$, where $G_0 = 1/12.9\,\mathrm{k}\Omega^{-1}$. The nanotube diameter is ∼1.5 nm and the distance between the contacts is 800 nm. From [Kon01].

to the theoretical maximum of $4e^2/h$ [Ana01]. Finally, a novel experiment observed the effect of the relative wave vectors of a nanotube and contact in determining the efficiency of electron transfer between them [Pau00]. This experiment showed that wave vector mismatch can cause the current to vary by more than an order of magnitude depending on the relative orientation of a nanotube on a graphite contact.

In contrast to the MWNT experiment discussed, values of conductance close to the theoretical maximum of$4e^2/h$ have been measured on SWNTs as shown in figure 11 [Kon01]. As the temperature is lowered, the conductance approaches $4e^2/h$. Both contacts in this experiment were made of titanium. Motivated by the experimental work of [Kon01], *ab initio* methods have been used to study which metal makes the best contact with nanotubes. In agreement with experiments, the theoretical studies [And00, Yan02, Liu03, Pal03] show that titanium forms the best contact when compared with other metals such as Au, Al, Ni, Fe and Co.

The results discussed above show that nanotubes are excellent wires, with near-perfect experimentally measured conductances. At first sight this is surprising because surface scattering, disorder, defects and phonon scattering, which lead to a decrease in conductance, seem ineffective. The reasons for this are the following.

(i) The acoustic phonon mean free paths are longer than a micron [Par04]. The dominant scattering mechanisms are due to zone boundary and optical phonons with energies of approximately 160 and 200 meV; but scattering with these phonons at room temperature is ineffective at small biases.

(ii) The nanotube has a crystalline surface without disordered boundaries. In a silicon field effect transistor, there is significant scattering of electrons due to the disordered nature of the Si–$SiO_2$ interface.

(iii) The crossing points of metallic nanotubes correspond to the reciprocal lattice wave vector $|K| = 4\pi/3|a_1|$ of the underlying graphene sheet, where $|a_1|$ is the length of the real space lattice vector of graphene (figure 2(*a*)). The two different crossing subbands of metallic nanotubes (figure 9) correspond to these $K$ points in the graphene sheet. As a result, any potential that is long-ranged compared with $a_1$ will not effectively couple the two crossing subbands because of a lack of wave vector components in the reciprocal space [And98].

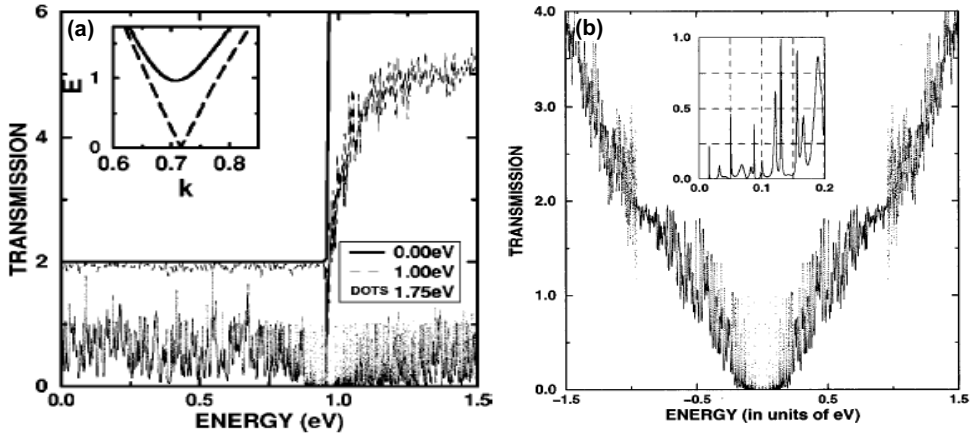


**Figure 12.** (*a*) Effects of disorder potential on the transmission of a metallic nanotube. The significant features here are the robustness of the transmission around the zero of energy, as the strength of disorder is increased, and the dip in transmission at energies close to the beginning of the second subband. The inset shows energy versus wave vector for the first (——) and the second (- - - -) subband. The velocity of electrons at the minima of the second subband is zero, and the corresponding density of states is large, which causes the transmission to dip. Calculations were done on a (10,10) nanotube with disorder distributed over a length of 1000 Å. (*b*) The transmission versus energy of a (10,10) CNT with ten vacancies sprinkled randomly along a length of 1000 Å. The main prediction here is the opening of a transmission gap around the zero of energy. Inset: comparison of the transmission for tubes of lengths 1000 Å (——) and 140 Å (- - - -) with ten scatterers, in each case. The transmission gap is larger for the larger defect density and the sharp resonances close to the zero of energy are suppressed with increasing defect density. From [Ana98].

(iv) The electrons in the crossing subbands have a large velocity of $8 \times 10^5$ m s$^{-1}$ at the Fermi energy. This, coupled with the small final density of states for scattering (as there are only two subbands at the Fermi energy), makes the reflection probability due to disorder/defects small [Ana98, Whi98].

The robustness of transport in the crossing subbands is illustrated by considering disorder in the on-site potential at every atomic site. The disorder potential is generated using a random number generator with a maximum value of 1 eV (dashed line) and 1.75 eV (dotted line). The change in transmission due to the disorder potential is shown in figure 12(*a*). The case without disorder corresponds to the solid line, where the transmission is two at the Fermi energy. The main feature of this figure is that the transmission around the Fermi energy is not significantly affected by disorder. The disorder of 1.75 eV is comparable to the hopping parameter of 2.77 eV between carbon atoms, yet the average transmission at the Fermi energy is approximately 0.75. This robustness of the small bias conductance is due to item (iv) discussed above. A second noteworthy feature of figure 12(*a*) is that the transmission dips to low values when the first non-crossing subband opens around $E = 0.85$ eV. This is because of coupling between the high velocity states of the crossing subband with low velocity states of the non-crossing subband. Note that the final density of states for scattering is large when the non-crossing subband opens due to a van Hove singularity. One defect that can significantly change transmission in the crossing subband of a metallic nanotube is a vacancy—a missing carbon atom or an atom with an onsite potential that is significantly different from that of carbon [Ana98, Cho00]. Figure 12(*b*) shows that ten vacancies randomly distributed along the length of a 1000 Å long nanotube can make the transmission negligible at some energies. While the energy window

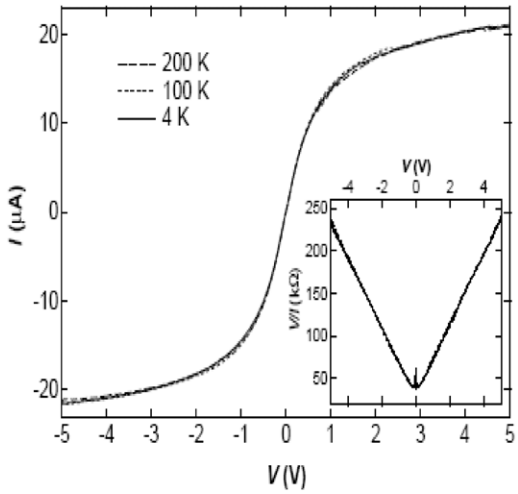


**Figure 13.** Current versus applied bias of a metallic nanotube at different temperatures. The differential conductance is largest at zero bias and saturates to much lower values at high biases. The inset shows resistance versus bias. From [Yao00].

where the transmission diminishes the most lies in the crossing subbands, the exact location depends on the model used [Cho00]. More recently, there has been experimental evidence that the conductance of metallic nanotubes is significantly affected when bombarded by argon ions; modelling has shown that a potential mechanism is the scattering from vacancies created by ion bombardment [Gom05].

### *2.3. High bias transport*

At high biases, the current carrying capacity of CNTs is significantly affected by electron–phonon scattering. Figure 13 shows the experimentally measured current–voltage characteristics of a small diameter nanotube. The conductance is largest at zero bias and decreases with an increase in bias. The inset of figure 13 shows the increase in resistance of a small diameter (15 Å) metallic nanotube with increase in bias.

To understand the experimentally observed current–voltage characteristics, we will now discuss the flow of electrons incident from the contact into both the crossing and non-crossing subbands of nanotubes. Consider an electron incident into a 'valence band' (non-crossing subband) of the nanotube from the left contact (figure 14). This electron can either tunnel to the 'conduction band' (non-crossing subband) with the same symmetry (dashed line) or be Bragg-reflected back into the left contact (dotted line). The barrier for Zener tunnelling in the non-crossing subband is $\Delta E_{\mathrm{NC}}$, which is the energy of the band bottom of the non-crossing subband, and the barrier width depends on the potential profile in the nanotube. As the barrier height, $\Delta E_{\mathrm{NC}}$, increases with decrease in nanotube diameter, it turns out that the non-crossing subbands of small diameter nanotubes do not carry any current [Ana00, Svi05]. This leaves only the crossing subbands to carry current (dashed line of figure 14).

The electron–phonon interaction is significant only for zone boundary and optical phonons that have energies of 160 meV and 200 meV, respectively. At biases comparable to 160 mV, an electron can lose energy due to spontaneous emission of zone boundary phonons. The mean free path of this process is small (10–20 Å) and as a result, the conductance decreases appreciably due to reflection of electrons. If one assumes that all electrons incident from

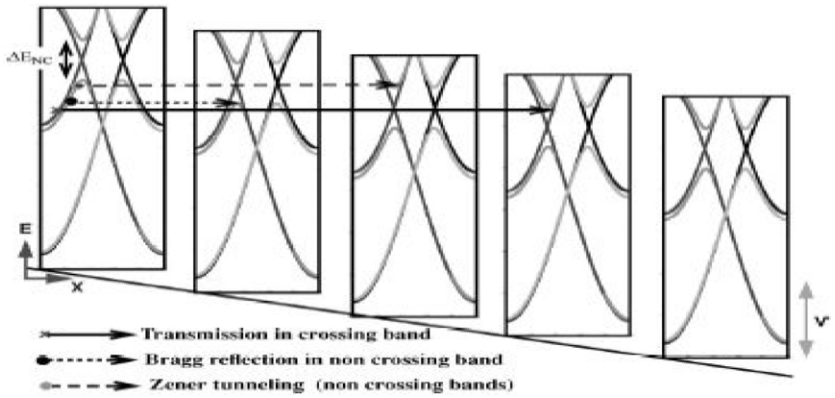


**Figure 14.** Each rectangular box is a plot of energy versus wave vector, with the subband bottom equal to the electrostatic potential. Only a few subbands are shown for the sake of clarity. The three processes shown are direct transmission (——) Bragg reflection (· · · · · ·) and intersubband Zener tunnelling (- - - -). From [Ana00].

the left contact with energy 160 meV larger than the drain side Fermi energy are reflected by phonon emission then the maximum current that flows in a long nanotube (many mean free paths) at large biases will be approximately

$$I = \frac{4e^2}{h} 160\,\mathrm{mV} = 30\,\mu\mathrm{A}. \tag{2.3.1}$$

A number of experiments have now reported currents comparable to 30 $\mu$A in long nanotubes [Yao00, Col01, Par04]. The computed current–voltage characteristics in the ballistic limit and with electron–phonon interaction is shown in figure 15. At small biases, the conductance $\mathrm{d}I/\mathrm{d}V$ is nearly $4e^2/h$, independent of nanotube length, corresponding to ballistic charge transport in the crossing subbands. The conductance value does not depend on the nanotube diameter because there are two subbands at the Fermi energy, independent of the diameter. As the bias increases, the current carrying capacity and differential conductance are length-dependent. The longest nanotube considered (length of 213 nm) is considerably longer than the mean free path of about 10 nm. The computed current for this nanotube is about 30 $\mu A$ at a bias of 1 V, in agreement with equation (2.3.1). As the length of the nanotube decreases, the current carrying capacity increases and approaches the ballistic limit (dashed line) in figure 15.

It is worth mentioning that the experimentally measured mean free paths of nanotubes are nearly five times smaller than the theoretical one. [Par04] theoretically estimated the mean free path due to optical and zone boundary scattering to be about 50 nm but found that the experimental data could be explained only if a net mean free path of 10 nm was assumed. The reason for this disparity in theoretical and experimental mean free paths is unclear. An interesting possibility is that the emitted phonons cannot easily dissipate into the environment, resulting in hot phonons, and the smaller experimentally observed mean free path.

In contrast to small diameter nanotubes, large diameter nanotubes show an increase in differential conductance with applied bias [Fra98, Lia04]. Figure 16 shows the experimentally measured current and conductance versus bias for a nanotube with a diameter of 15.6 nm [Lia04]. The low bias conductance is $0.4G_0$ instead of maximum of $2G_0$. More importantly, the conductance increases with applied bias, a feature also seen in [Fra98]. This is qualitatively different from the case of small diameter nanotubes where the conductance decreases with increase in bias (figure 13). There are many potential reasons for the increase in conductance

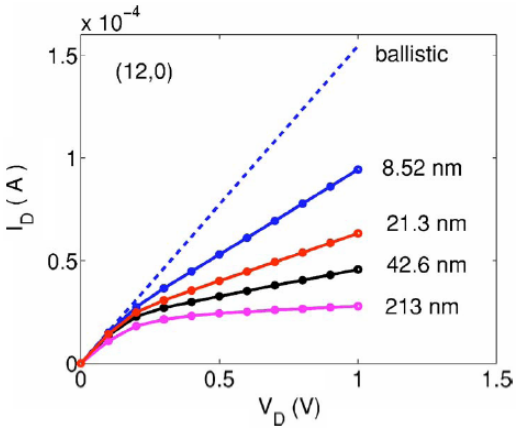


**Figure 15.** Computed current–voltage characteristics in the ballistic limit (- - - -) and with electron–phonon scattering for various lengths. For the longest nanotube considered (213 nm), the current is close to 30 $\mu$A, as given by equation (2.3.1). The current approaches the ballistic limit as the nanotube length decreases. From [Svi05].

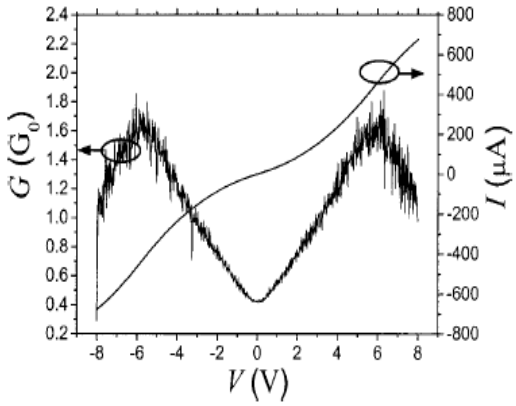


**Figure 16.** Observed $I$–$V$ curve of a single MWNT in the bias range from −8 to 8 V (right axis). The current reaches 675 $\mu$A at the bias of 8 V. The conductance around zero bias is $0.4G_0$ and increases linearly until an applied bias of 5.8 V. The MWNT has more than 15 shells and diameters and lengths of approximately 15.6 nm and 500 nm, respectively. From [Lia04].

with bias seen in large diameter MWNTs. One possibility is that the inner walls of the MWNT carry current, in addition to the outermost wall, as the bias increases. Recent theoretical work found that this mechanism is unlikely [Yoo02]. Another reason for the increase in conductance with applied bias could be Zener tunnelling discussed in figure 14 [Ana00]. The barrier for Zener tunnelling, $\Delta E_{\mathrm{NC}}$, in figure 14 decreases with an increase in nanotube diameter. As a result, the probability of Zener tunnelling increases with increase in nanotube diameter. Self-consistent calculations of the current–voltage characteristics of short nanotubes also showed a significant diameter dependence of the conductance versus bias arising due to tunnelling into non-crossing/semiconducting subbands [Ana00, Svi05]. Recent experiments seem to support the modelling results [Lia04, Bou04].

Finally, we discuss the electrostatic potential drop in CNTs at low and high biases, which is a quantity that is of relevance to both experiments and modelling. We will limit the discussion

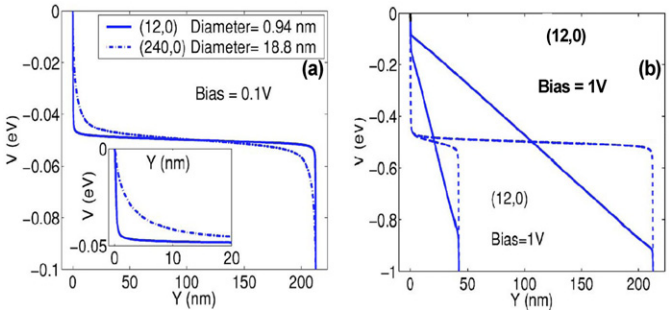


**Figure 17.** Electrostatic potential versus length along nanotube axis. (*a*) Low bias potential versus position for (12,0) and (240,0) nanotubes, which have diameters of 0.94 nm and 18.8 nm, respectively. The applied bias is 100 mV. The screening for the large-diameter nanotube is significantly poorer. The inset magnifies the potential close to the nanotube–contact interface, showing that in contrast to the nanotube bulk the electric field is smaller at the edges when the diameter is larger (density of states is smaller). The nanotube length is 213 nm. (*b*) The potential as a function of position is shown for (12,0) nanotubes of lengths 42.6 and 213 nm in the presence of scattering (——). The potential profile in the ballistic limit (- - - -) is shown for comparison. From [Svi05].

here to perfect coupling between the nanotube and contacts. The nanotube conductance is then limited by the number of subbands carrying current (equation (2.2.1)) and scattering due to electron–phonon interaction inside the nanotube. Note that an additional resistance at the nanotube–contact interface will cause the applied bias to drop across this resistance, in addition to the drop across the nanotube.

At low bias, smaller than the energy of optical and zone boundary phonons (less than 160 meV), electron–phonon scattering is suppressed, and hence defect-free nanotubes are essentially ballistic. In this low bias limit, the applied bias primarily drops across the two ends of the nanotube as shown in figure 17(*a*). Interestingly, even though the nanotube is ballistic, the electric field depends on the tube diameter. The electric field at the centre of the nanotube increases with an increase in diameter because the density of states per atom decreases with the increase in diameter (equation (1.9)). When the applied bias increases to allow the emission of optical and zone boundary phonons, the electrostatic potential drops uniformly over the length of the nanotube provided that the nanotube length is many times the mean free path. The potential drop in figure 17(*b*) corresponds to this case.

### *2.4. Quantum capacitance and inductance of nanotubes*

In this section, we discuss the concepts of quantum capacitance and inductance associated with a CNT and then describe how they impact the velocity of signal propagation in nanotubes. In conductors, there are two sources of energy associated with the addition of charge (capacitance) and current flow (inductance): classical and quantum. The classical source of capacitance ($C$) and inductance ($L$) follows from electrodynamics, and they are related to energy by

$$E = \frac{1}{2}CV^2 = \frac{Q^2}{2C} \tag{2.4.1}$$

and

$$E = \frac{1}{2}LI^2, \tag{2.4.2}$$

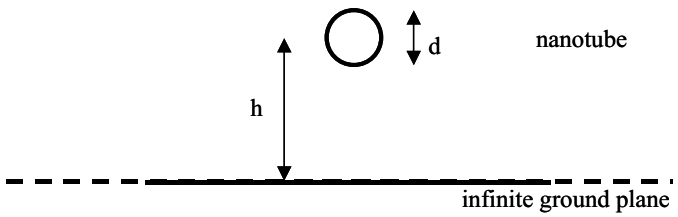


**Figure 18.** Metallic nanotube over a ground plane.

where $Q$ and $I$ are charge and current, respectively. The quantum source of capacitance and inductance arises because the charge added to a conductor depends on the Fermi energy and the density of states.

*Quantum capacitance.* Consider a nanotube in equilibrium at an electrostatic potential $V_0$. If the electrostatic potential changes to $V_0 + \delta V$ then the change in charge $\delta Q$ per unit length is given by

$$\delta Q = e \int \mathrm{d}E\, D(E)[f(E-\mu) - f(E - e\delta V - \mu)]. \tag{2.4.3}$$

Assuming that the density of states per unit length $D(E)$ does not change around the Fermi energy, we obtain

$$\delta Q = e^2 D(\mu)\delta V. \tag{2.4.4}$$

The quantum capacitance is then given by

$$C_{\mathrm{Q}} = \frac{\delta Q}{\delta V} = e^2 D(\mu). \tag{2.4.5}$$

For a metallic CNT, the density of states per unit length at the Fermi energy is $D(E) = 4/\pi v_{\mathrm{F}}$ (factor of 4 corresponds to two spins and two subbands). Using this, we find that the quantum capacitance per unit length is [Boc99, Bur02]

$$C_{\mathrm{Q}} = \frac{4e^2}{\pi \hbar v_{\mathrm{F}}} \sim 0.4\,\mathrm{aF\,nm^{-1}}. \tag{2.4.6}$$

To compare the quantum capacitance with the electrostatic capacitance we consider a metallic wire of diameter $d$ above a ground plane at a distance $h$ (figure 18). The electrostatic capacitance is

$$C_{\mathrm{E}} = \frac{2\pi\varepsilon}{\ln(2h/d)}, \tag{2.4.7}$$

where $\varepsilon$ is the dielectric constant of the medium surrounding the CNT. For a nanotube with $d = 1.5\,\mathrm{nm}$ and $h = 1.5\,\mathrm{nm}$, the electrostatic capacitance for $\varepsilon = 4$ is

$$C_{\mathrm{E}} \sim 0.1\,\mathrm{aF\,nm^{-1}},$$

which is comparable to the quantum capacitance in (2.4.6). Thus both the classical and quantum capacitance need to be taken into account when analysing the electrical properties of CNTs.

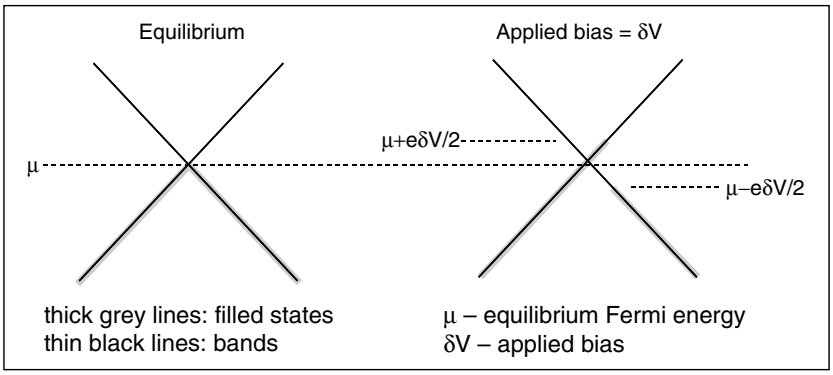


**Figure 19.** The left panel shows the occupied states at equilibrium. The right panel shows the occupied states in the presence of an applied bias, $\delta V$.

*Kinetic inductance.* The physical origin of kinetic inductance ($E_k$) is the excess kinetic energy associated with current flow [Boc99,Tar01,Bur02]. This is illustrated in figure 19, which shows ballistic electrons flowing between the source ($\mu+\delta V/2$) and drain ($\mu-\delta V/2$) Fermi energies, where $\mu$ is the equilibrium Fermi energy. We make the following observations [Boc99]:

change in energy of electrons in bias window $\sim e\delta V/2$ and
average number of electrons in bias window $\sim(D(\mu)/2)(e\delta V/2)$.

From the above two expressions, we see that the

excess kinetic energy $\sim 1/8 D(\mu)(e\delta V)^2$,
current ($I$) $\sim(4e^2/h)\delta V$, where $\delta V \sim (\mu_L - \mu_R)/e$.

The expression for average number of electrons has the density of states divided by two because only the right moving carriers are present in the bias window. Equating the expression for excess kinetic energy to an inductive energy $(1/2)L_K I^2$, the kinetic inductance ($L_K$) is

$$L_K = \frac{\pi^2\hbar^2 D(\mu)}{16e^2}. \tag{2.4.8}$$

Using the expression for the density of states at the Fermi energy of metallic CNTs $D(\mu) = 4/\pi\hbar v_F$, the kinetic inductance is

$$L_K = \frac{\pi}{4e^2 v_F}. \tag{2.4.9}$$

Substituting the Fermi velocity $v_F = 8 \times 10^5\,\mathrm{m\,s^{-1}}$ in the above expression, the kinetic inductance of metallic CNTs is

$$L_K \sim 4\,\mathrm{pH\,nm^{-1}}.$$

The magnetic inductance of a nanotube over a ground plane (figure 18) is

$$L_m = \frac{\mu}{2\pi}\cosh^{-1}\left(\frac{2h}{d}\right). \tag{2.4.10}$$

For $d = h = 1.5\,\mathrm{nm}$, the magnetic inductance, $L_m \sim 5.5 \times 10^{-4}\,\mathrm{pH\,nm^{-1}}$. The kinetic inductance is about ten thousand times larger than the magnetic inductance and hence cannot be neglected in the modelling of CNT interconnects. It would take over 10 000 nanotubes arranged in parallel for the magnetic inductance to become equal to the kinetic inductance.

The above discussion of kinetic inductance assumed ballistic transport of electrons, which is truly valid only at low biases. At biases larger than 160 mV, scattering due to optical phonons decreases the current and leads to the relaxation of the incident carriers, causing a decrease in the kinetic inductance for nanotubes much longer than the mean free path. For a semiclassical treatment of quantum inductance based on the Boltzmann equation, see [Sal05].

*Velocity of wave propagation.* The large value of kinetic inductance has an important effect on the speed at which signals are propagated in a transmission line consisting of a single nanotube (figure 18). The wave velocity for signal transmission in the nanotube transmission line is

$$\text{Wave velocity} = \sqrt{\frac{1}{LC}} \sim \sqrt{\frac{1}{L_K}\left(\frac{1}{C_E} + \frac{1}{C_Q}\right)} \tag{2.4.11}$$

When the quantum capacitance is much smaller than the electrostatic capacitance the wave velocity for propagation of an electromagnetic signal is (using equations (2.4.6) and (2.4.9))

$$\text{Wave velocity} \sim \sqrt{\frac{1}{L_K C_Q}} = v_F, \tag{2.4.12}$$

which is equal to the Fermi velocity of electrons.

If there are $N$ nanotubes in parallel then the expression for the velocity of signal propagation is

$$\text{Wave velocity} = \sqrt{\frac{1}{L_K + NL_M}\left(\frac{N}{C_E} + \frac{1}{C_Q}\right)}, \tag{2.4.13}$$

which reduces to the classical expression $\sqrt{1/L_M C_E}$, when the magnetic inductance and electrostatic capacitance dominate.

## 3. Physics of nanotube/metal contacts

### *3.1. Introduction*

Contacts play a crucial role in electronic devices, and much work has been devoted to understanding and controlling the properties of contacts. For example, in traditional contacts between metals and semiconductors, a body of experimental and theoretical work has shown that Fermi level pinning usually dominates, leading to a Schottky barrier at the contact. Figure 20 shows the measured [Sze81] Schottky barrier height for contacts between Si and various metals.

Clearly, the barrier height is essentially independent of the metal workfunction. A simple model where the barrier height is given by the difference between the semiconductor electron affinity $\chi_s$, and the metal workfunction, $\chi_m$,

$$\phi_{b0} = \chi_m - \chi_s \tag{3.1.1}$$

fails to describe the experimentally measured barrier heights.

The nearly constant barrier heights can be explained using the concept of Fermi level pinning. While an infinitely large semiconductor has a true electronic bandgap, the surface at the metal/semiconductor interface introduces boundary conditions in the solutions of Schrodinger's equation, thus allowing electronic states to appear in the semiconductor bandgap. These so-called metal-induced gap states (MIGS) decay exponentially away from the interface

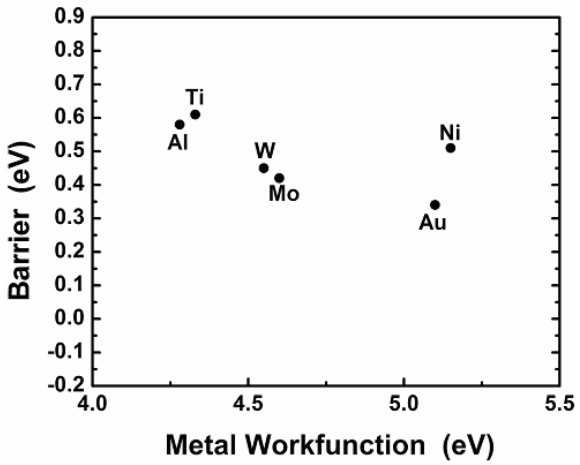


**Figure 20.** Measured Schottky barrier heights for traditional contacts between silicon and various metals.

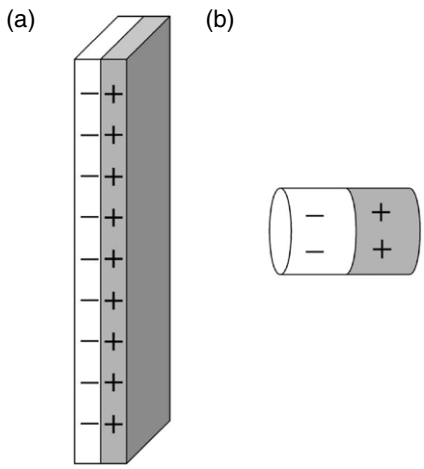


**Figure 21.** (*a*) Charge dipole sheet due to MIGS at a traditional metal/semiconductor contact. (*b*) In contrast to (*a*), at a nanotube/metal contact, the MIGS give rise to a charge dipole ring.

and locally change the 'neutrality' level in the semiconductor, i.e. the position of the Fermi level where the charge near the semiconductor surface vanishes. This can be modelled [Leo00a] as a charge:

$$\sigma(z) = D_0(E_N - E_F)e^{-qz}, \tag{3.1.2}$$

where $D_0$ is the density of MIGS, $E_N$ is the position of the neutrality level, $E_F$ is the metal Fermi level and $q$ determines the distance over which the MIGS decay away from the interface. Because the charge is localized over a distance $1/q$ from the interface and because of image charges in the metal, the charge due to the MIGS can be viewed as creating a dipole sheet, as shown in figure 21.

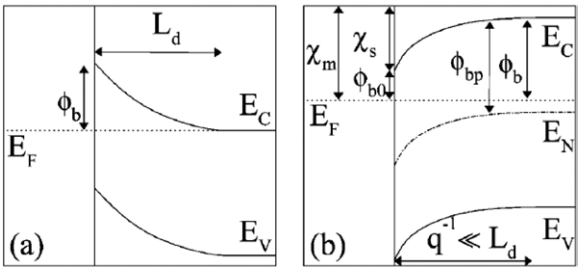


**Figure 22.** (*a*) The band-bending for a traditional doped semiconductor/metal junction. The band-bending occurs over a length scale $L_d$, which is the Debye length. (*b*) The near interface region, i.e. distances much smaller than $L_d$, is shown. From [Leo00a].

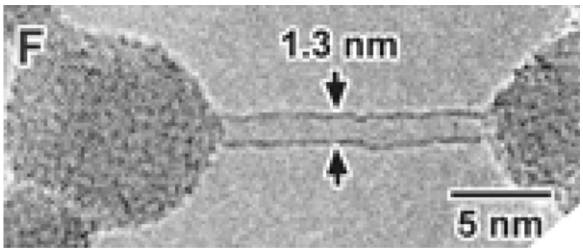


**Figure 23.** TEM image of a SiC/Nanotube contact. From [Zha99].

The presence of this charge near the interface will change the electrostatic potential according to

$$V(z) = \int K(z - z')\sigma(z')\,\mathrm{d}z', \tag{3.1.3}$$

where $K(z)$ is the electrostatic kernel. For the dipole sheet with infinite cross-sectional area, the potential shift is a constant far from the interface, such that the metal Fermi level is located at the charge neutrality level. Thus, the barrier height is increased to

$$\phi_b = \phi_b^0 + E_F - E_N. \tag{3.1.4}$$

For a charge neutrality level in the middle of the semiconductor bandgap, the metal Fermi level will be located at midgap, thus giving rise to a barrier equal to half the semiconductor bandgap, as shown in figure 22. This idealized limit agrees relatively well with the data presented in figure 20.

The presence of the Schottky barrier implies that electronic transport across the contact is dominated by thermionic emission over the Schottky barrier, significantly increasing the contact resistance. The key questions are: how is the physics modified for nanotube/metal contacts? What are the implications for electron transport?

To address these questions, it is important to note a key difference between nanotube/metal contacts and traditional contacts. While traditional contacts are essentially planar, nanotube contacts can show various structures. Figure 23 shows a contact between a nanotube and SiC, where the nanotube is 'end-bonded' to the metal [Zha99]. Figure 24 shows a different situation where the nanotube lies on a metal surface and is 'side-contacted'. The different contact geometries and the reduced dimensionality of nanotubes can have a strong effect on the contact behaviour, as we now discuss.

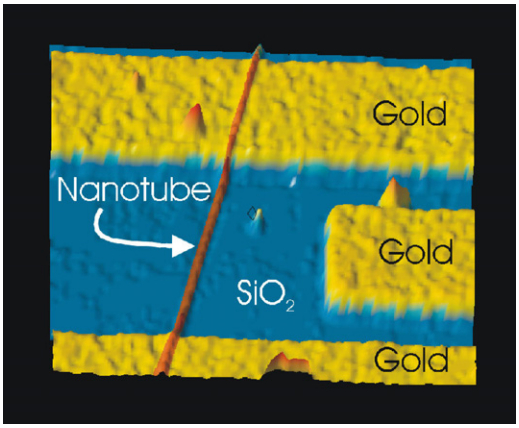


**Figure 24.** CNT forming 'side-contacts' on gold electrodes. Figure courtesy of R Martel.

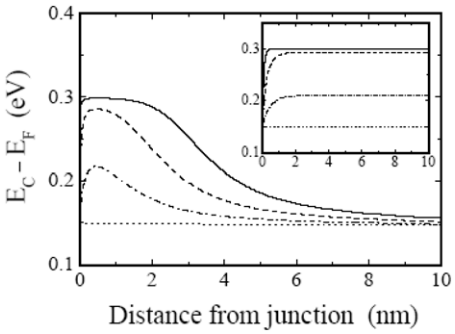


**Figure 25.** Band-bending due to MIGS at a nanotube/metal contact. From [Leo00a].

### *3.2. Role of Fermi level pinning in end-bonded contacts*

The contact in figure 23 is similar to traditional planar contacts in the sense that the semiconducting nanotube terminates at the metal. Thus, it is interesting to explore the role of Fermi level pinning in such contacts [Leo00a].

While the model for the induced charge due to MIGS still applies (equation (3.1.2)), the MIGS charge takes the form of a dipole ring rather than a dipole sheet, as shown in figure 21. This has a critical effect on the electrostatic potential and the resulting band-bending. While the electrostatic potential is a constant far from a dipole sheet, it decays as the third power of distance far from a dipole ring. Thus, in the CNT contact, any potential shift near the interface will decay rapidly. Self-consistent calculations of equations (3.1.2) and (3.1.3) show that the potential shift essentially disappears within a few nanometres away from the interface as shown in figure 25 [Leo00a]. Because the barrier is only a few nanometres wide, electrons can efficiently tunnel through the extra barrier due to Fermi level pinning. Thus, in contrast to traditional semiconductor/metal contacts, Fermi level pinning plays a minor role in end-bonded CNT/metal contacts. An important consequence of this is that the type of metal used to contact the CNT has a strong influence on the properties of the contacts, as we now discuss.

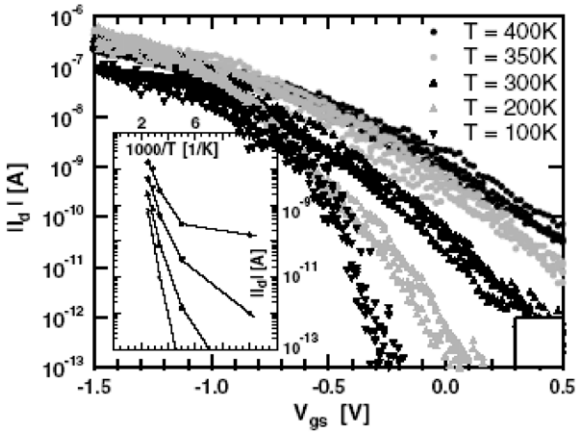


**Figure 26.** Inset: measured current across a nanotube/Ti contact as a function of inverse temperature, indicating thermionic-like behaviour over a Schottky barrier. From [App04].

### *3.3. Schottky barriers at nanotube/metal contacts*

The evidence of Schottky barriers at contacts such as the one in figure 23 is intimately related to the behaviour of CNT transistors with such contacts, as will be discussed in section 4. Perhaps the simplest way to illustrate the presence of a Schottky barrier at these contacts is to measure the temperature dependence of the current. In the presence of a SB, the current is thermally activated above the barrier, and thus the current increases with temperature. The inset in figure 26 shows precisely this behaviour. [Yam04] also discusses the role of contacts in clarifying the physics in some nanotube experiments.

### *3.4. Ohmic contacts to nanotubes*

According to the discussion in section 3.2, the barrier at CNT/metal contacts should be well described by $\phi_{b0} = \chi_m - \chi_s$. For a typical CNT with a bandgap of 0.6 eV, and for the CNT midgap 4.5 eV below the vaccum level [Ago00], metal workfunctions larger than 4.8 eV (or less than 4.2 eV) would thus lead to a negative Shottky barrier, i.e. the metal contacts the CNT in the valence (conduction) band, giving an Ohmic contact. Thus, one may expect that Au (5.5 eV) and Pd (5.1 eV) would give Ohmic contacts.

Figure 27 shows the measured conductance for a CNT transistor with Pd contacts [Jav03]. As seen in the figure, the device conductance is close to the maximum conductance of $4e^2/h$, thus indicating that no barrier exists at the contact. This can be further confirmed by studying the temperature dependence of the conductance. As the right panel in figure 27 shows, the conductance increases with a reduction in the temperature. This temperature dependence is the opposite of what happens in Schottky barrier contacts as illustrated in figure 26.

Experiments using an atomic force microscope tip as an electrical scanning probe along the CNT have also observed Ohmic behaviour in Au contacts [Yai04]. Figure 28 shows the current between the tip and the contact electrode before and after annealing the contact. Clearly, the behaviour is rectifying before annealing, indicating the presence of a Schottky barrier. After annealing, the current–voltage curve is linear showing that the contact is now Ohmic. This result was also confirmed by cooling the device, which showed an increase in conductance.

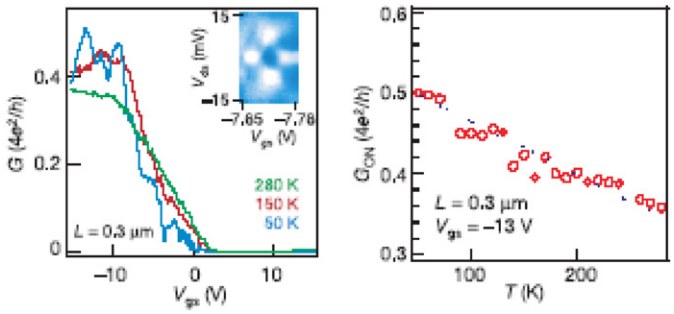


**Figure 27.** (Left panel) Measured conductance as a function of gate voltage in a CNT transistor. The largest conductance measured is near the maximum possible value. The right panel shows the conductance as a function of temperature, with a behaviour opposite to that in the Schottky barrier device of figure 26. From [Jav03].

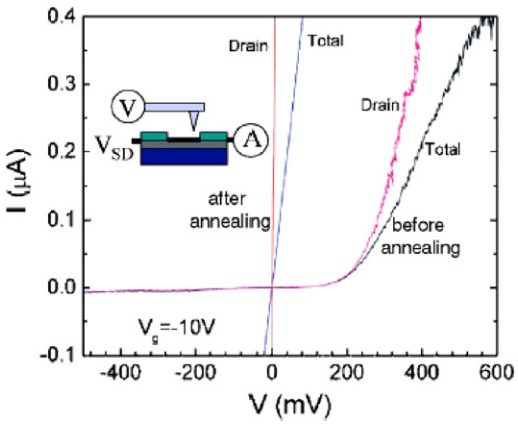


**Figure 28.** Current/voltage characteristics of a semiconducting nanotube contacting two metal electrodes, probed with an AFM tip. From [Yai04].

### *3.5. Metal/oxide/nanotube contacts*

While most of the research on the properties of the nanotube/metal contacts has focused on fabricating the Ohmic contacts to obtain the lowest possible contact resistance, for electrical insulation and tunnelling applications, it is important to develop contacts that have high resistance. Figure 29 shows nanotubes between Pd electrodes but where the Pd electrodes were exposed to $O_2$ plasma [Tal04]. As the 'sweep 1' curve in figure 29 shows, the current across such contacts is extremely small, and the properties of the contact are very stable up to moderate voltages. Auger spectroscopy and theoretical modelling have shown that the oxide is only about 2 nm thick. Thus, such ultrathin PdO oxides are good candidates for gate insulator materials. A particularly intriguing feature of these Pd/PdO/nanotube contacts is an irreversible transition to a high conducting behaviour as large voltages are applied. As figure 29 indicates, for voltages larger than about 2.5 V, the current across the contacts increases dramatically and irreversibly, leading eventually to low contact resistance.

One may imagine using this mechanism in a transistor fabrication method where the nanotube is laid across three Pd electrodes covered with PdO and applying a large voltage

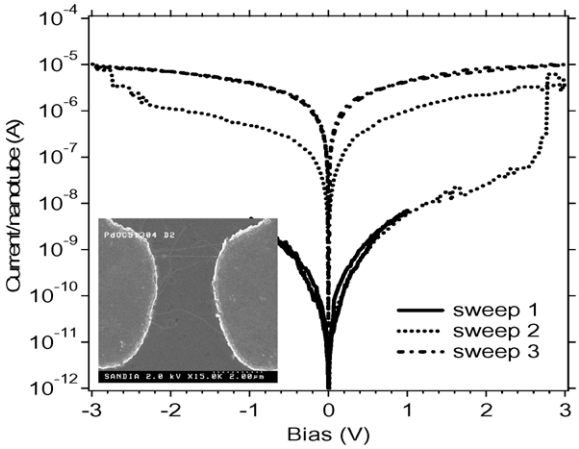


**Figure 29.** SEM image and $I/V$ curves for a device with Pd/PdO/NT contacts. Application of a large voltage transforms the contacts from very low to high conductance. From [Tal04].

across the source and drain to 'form' the source and drain contacts while leaving the gate floating.

## 4. Electronic devices with semiconducting nanotubes

### *4.1. Introduction*

Given their semiconducting character and their high aspect ratio and structural robustness, it is natural to ask if CNTs can be used as current carrying elements in nanoscale electronic devices. Indeed, there have been many demonstrations of such devices, ranging from two-terminal rectifiers to field-effect transistors. While some of these devices bear a resemblance to traditional devices, this section emphasizes the much different physics that governs the operation of the CNT devices.

### *4.2. Rectifiers*

Rectifiers are simple two-terminal devices that allow current to flow for only one polarity of the applied voltage, the simplest examples being the p–n junction diodes and the Schottky diodes. While these are simple devices, they are excellent systems to study the differences between the CNT-based devices and the conventional devices.

*4.2.1. Experimental realizations of CNT p–n junctions.* There are many possible strategies to dope nanotubes in order to make p–n junctions. Examples include substitution of B and N in the carbon lattice, doping by charge transfer from electrodes, atoms or molecules or electrostatic control of the band bending. Figure 30 shows one of the strategies that has been implemented to fabricate such a device [Zho00]. The method hinges on the fact that the synthesized CNTs are predominantly p-type. Thus, it is only necessary to reverse the doping on one side of the CNT to obtain a p–n junction. This can be accomplished by protecting half of the CNT with PMMA and exposing the uncovered half to potassium, which is an electron donor. The associated current–voltage curve for such a device (figure 30) shows similarities with an Esaki diode, i.e. it shows negative differential resistance.

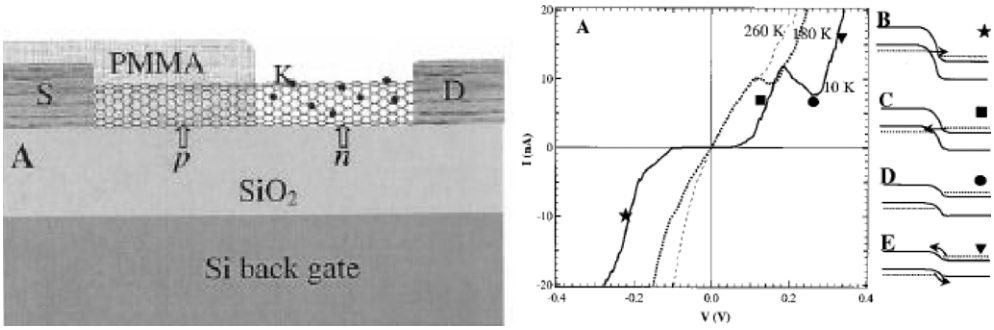


**Figure 30.** Schematic of chemically doped CNT p–n junction and the associated $I$–$V$ curve. From [Zho00].

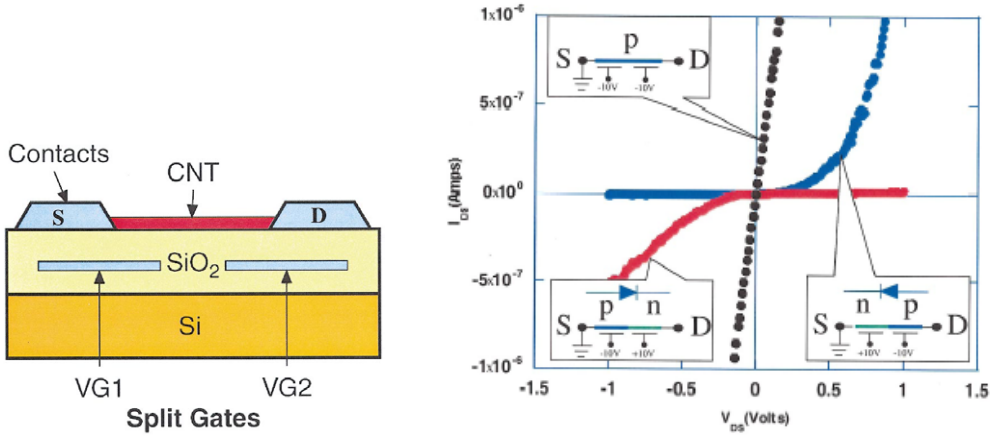


**Figure 31.** Split gate structure to create a CNT p–n junction without the need to dope the CNT. From [Lee04].

The role of dopants in p–n junctions is to create an electrostatic potential step at the junction. In traditional planar devices doping is essentially the only way to generate such a potential step. In CNTs, however, one can take advantage of the quasi-one-dimensional geometry and use an external electrostatic potential to form the p–n junction. An example of this strategy [Lee04] using a buried split gate structure is shown in figure 31. The advantages of this technique are that no chemical doping of the CNT is required, and that the device can be operated in several different modes. The right panel in figure 31 shows the $I$–$V$ curve for this device for three regimes of operation, allowing the transformation of the device from p–n to n–p and also shows transistor-like behaviour.

*4.2.2. Theory of CNT p–n junctions.* The behaviour of the CNT p–n junctions can be understood by performing self-consistent calculations of the charge and the electrostatic potential. The simplest model for the charge on the CNT is

$$\sigma(z) = \frac{e}{\varepsilon} f - \frac{e}{\varepsilon} \int D(E, z) F(E)\, \mathrm{d}E, \tag{4.2.1}$$

where $\varepsilon$ is the dielectric constant of the medium in which the CNT is embedded, $f$ is the doping fraction, $D(E, z)$ is the CNT density of states at position $z$ along the tube and $F(E)$ is

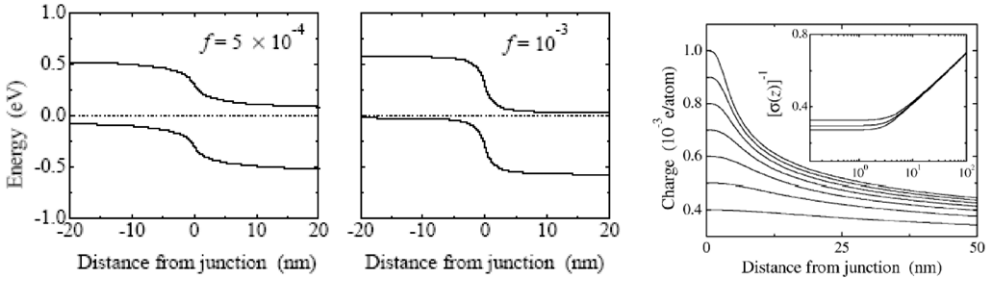


**Figure 32.** Calculated self-consistent band-bending and charge along a CNT p–n junction. From [Leo99].

the Fermi function. The density of states can be expressed as

$$D(E, z) = \frac{a\sqrt{3}}{\pi^2 R V_0} \frac{|E|}{\sqrt{(E + eV(z))^2 - (E_g/2)^2}}, \tag{4.2.2}$$

where $V(z)$ is the electrostatic potential along the CNT, $R$ is the CNT radius and $E_g$ is the bandgap. This expression for the spatial variation of the density of states is simply a rigid shift with the potential; while there are more sophisticated methods to calculate the actual density of states and the occupation of the states that enters in the calculation of the charge, equations (4.2.1) and (4.2.2) are sufficient to illustrate the general properties of the CNT p–n junctions.

The other equation necessary for the computations is the electrostatic potential:

$$V(z) = \int K(z - z')\sigma(z')\,\mathrm{d}z' \tag{4.2.3}$$

where $K(z - z')$ is the electrostatic potential for a hollow cylinder, $z$ is the coordinate along the axis of the nanotube and $\sigma$ is the charge per unit length. The procedure, therefore, is to solve equations (4.2.1), (4.2.2) and (4.2.3) self-consistently for a given doping on the CNT. Figure 32 shows results of such calculations for two doping fractions. Clearly, the band-bending in the CNT is similar to that observed in planar devices: a potential step at the junction and essentially flat bands away from the junction. The behaviour is quite different, however, if one looks at the charge distribution. In a planar device, there is a region of constant charge near the junction, and there is no charge outside that so-called depletion region. In CNTs, however, there is a significant charging away from the junction. In fact, the charge decays only logarithmically away from the junction. This difference between the planar and the CNT devices is again due to the different electrostatics of dipole sheets and dipole rings. In the planar device, having a dipole sheet at the junction is sufficient to ensure that the potential stays constant far away from the junction. For the dipole ring, however, the potential decays away from the junction. Thus, since the potential must be constant far away from the junction, the CNT must continuously add charge to keep the potential from falling.

While we discussed the long distance charging in the context of p–n junctions, Schottky junctions between the CNTs and the planar metals are also expected to show the same behaviour. This has been demonstrated experimentally. Figure 33 shows a scanning electron microscope (SEM) image of a CNT connecting two Au electrodes and the associated charge distribution away from the contact. The long distance charging is observed, as predicted theoretically.

The much different charge distribution and electrostatics in CNT junctions has a dramatic impact on device design. For example, in traditional devices, the height of the potential step

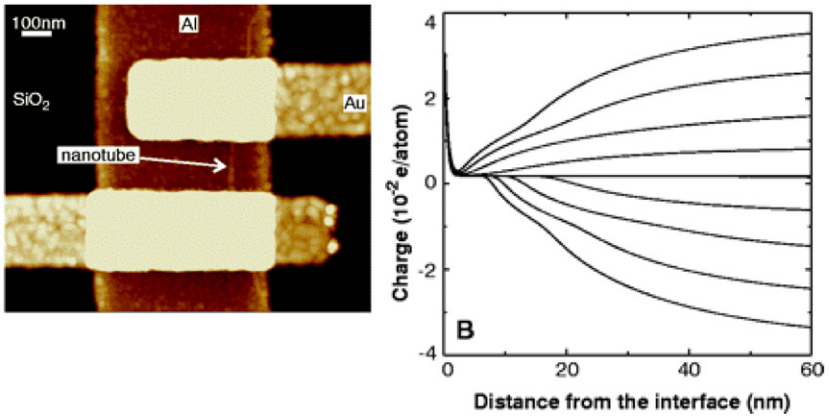


**Figure 33.** The left panel shows an SEM image of a CNT between two electrodes. The right panel shows the charge along the CNT, indicating the long-distance charge transfer from the electrodes. From [Bac01].

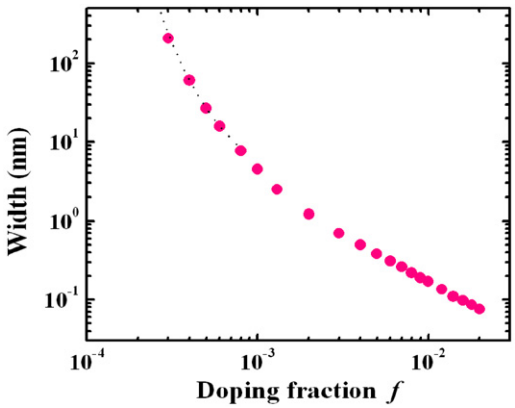


**Figure 34.** Calculated depletion width for a CNT p–n junction as a function of doping. From [Leo99].

can be tailored by changing the doping. The depletion width in such devices depends weakly on the doping, thus allowing for precise control of the device properties. For CNTs, however, the situation is quite different. Figure 34 shows the calculated depletion width for the CNT p–n junction as a function of doping. Clearly the depletion width is extremely sensitive to the doping, and thus fluctuations in dopant levels from device to device can significantly affect the device characteristics. Furthermore, at high doping, the depletion width is so small that tunnelling across the potential step prevents the device from rectifying. This tunnelling phenomenon is the basic operating principle behind the negative differential resistance devices and is observed in the experimental device of figure 30. It is thus interesting to model the properties of such devices. To do so requires computing the $I/V$ curve. This is done using the expression

$$I = \frac{4e^2}{h} \int T(E)[F_{\mathrm{L}}(E) - F_{\mathrm{R}}(E)]\,\mathrm{d}E, \tag{4.2.4}$$

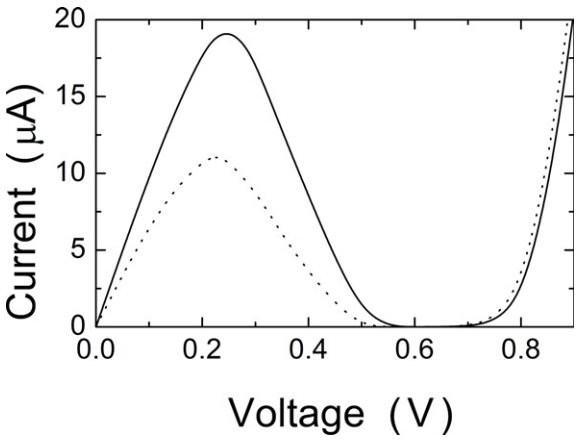


**Figure 35.** Calculated current–voltage curve for a CNT p–n junction with high doping. The current–voltage curve shows negative differential resistance. From [Leo00].

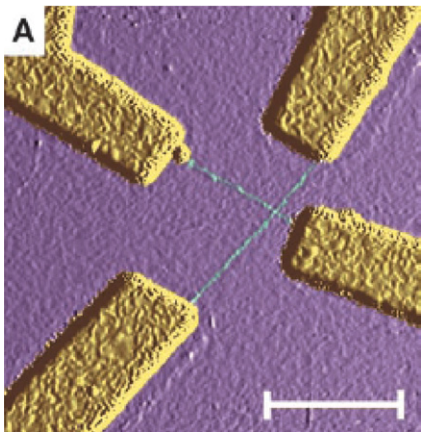


**Figure 36.** Nanotube devices made of two crossing nanotubes. From [Fuh00].

where $T(E)$ is the transmission probability across the junction and $F_{\mathrm{R}}(E)$ and $F_{\mathrm{L}}(E)$ are the Fermi functions in the right and left leads, respectively. Figure 35 shows the results of such calculations which indicate negative differential resistance.

*4.2.3. Metal-semiconductor junctions.* Sections 4.2.1 and 4.2.2 described the *intratube* nanotube p–n junctions, where rectification comes from the modulation of the doping within a single nanotube. Section 3 showed that contacts between nanotubes and metals can also act as Schottky diodes. In this section, we are concerned with metal-semiconductor rectifiers where both the metal and the semiconductor are CNTs. Such devices can be fabricated by combining two different nanotubes: figure 36 shows an experimental realization of one such device, consisting of two crossing nanotubes. Measurement of the individual conductance is used to determine the semiconducting or metallic character of each of the two CNTs. Figure 37 indicates that the current between the metallic and semiconducting CNTs (curve labelled MS) shows rectification. This rectification behaviour can be understood from the fact that the

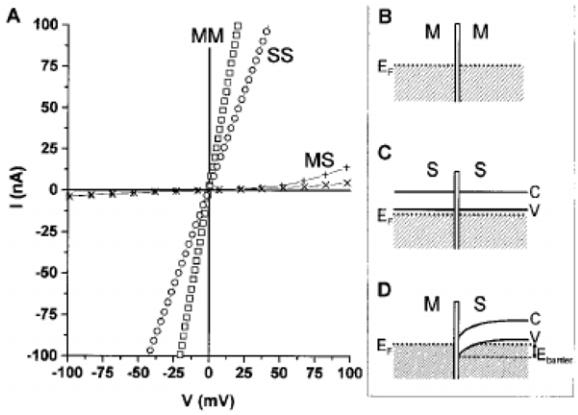


**Figure 37.** Measured $I$–$V$ curves for devices such as the one in figure 36. The metal-semiconductor (MS) junction shows rectifying behaviour, due to a Schottky barrier at the junction, as illustrated in panel (*d*) From [Fuh00].

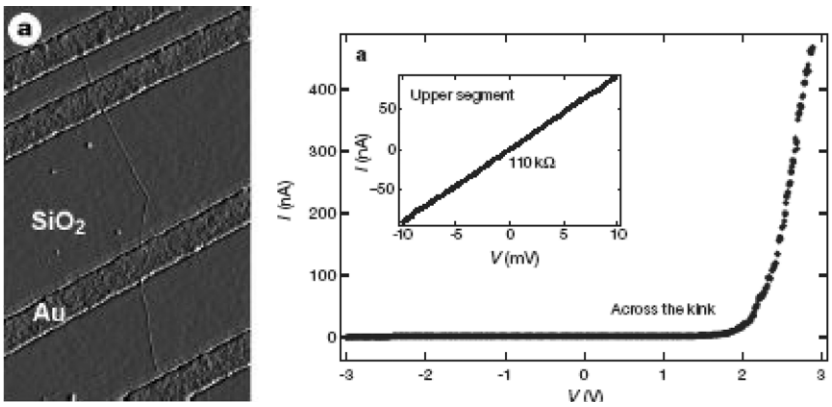


**Figure 38.** Intra-tube metal-semiconductor junction and the associated rectifying behaviour. From [Yao99].

bandgap in a semiconducting CNT arises from the opening of a symmetric gap around the Fermi points of a graphene sheet. Thus, the Fermi level is in the middle of the CNT bandgap and is at the same energy as the Fermi level in a metallic tube. This leads to the presence of a Schottky barrier at the crossing point between the two CNTs, as illustrated in figure 37.

The same Schottky barrier concept can be used to create *intra*-tube metal-semiconductor junctions. Figure 38 shows an image of a CNT in a four probe measurement configuration, with a kink between the middle electrodes. Two-probe measurements show that one end of the CNT is semiconducting, while the other end is metallic. Thus, the two segments of the CNT correspond to different chiralities, and the angle at which they meet is determined by the presence of topological defects which allow a seamless junction.

### *4.3. Field effect transistors*

Ever since its invention, the transistor has been the workhorse of the electronics industry. It is no surprise then that some of the initial devices made with CNTs have been transistors

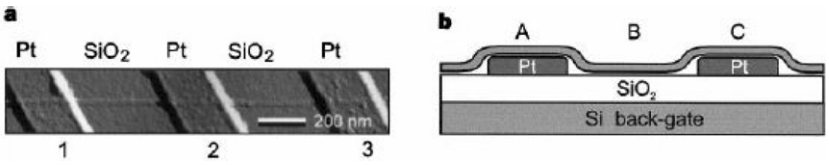


**Figure 39.** AFM image and sketch of the original CNT transistor. The transistor action is controlled by changing the voltage on the Si back gate. From [Tan98].

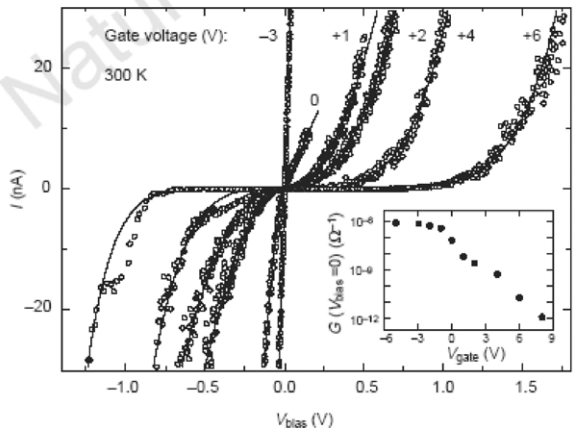


**Figure 40.** Current/voltage characteristics of an early CNT transistor. From [Tan98].

[Tan98, Mar98]. Figure 39 shows an AFM image of one of the early CNT transistors, which consists of a semiconducting CNT bridging two Pt electrodes and sitting on $SiO_2$ between the electrodes. A heavily doped Si substrate serves as a back gate, which controls the switching action of the transistor.

The drain current versus drain voltage characteristics of this transistor are shown in figure 40. In going from a gate voltage of −3 to +6 V, the device changes from a high to a low conductance, thus providing the switching action of the transistor.

Since this original device, there has been much experimental and theoretical progress in the understanding of the physics that governs the transistor action and in the improvement of the device performance. An important outcome of this work is the fact that the type of contact (Ohmic or Schottky) has a profound influence on the device behaviour.

*4.3.1. CNT transistors with Ohmic contacts.* As discussed in section 3, Ohmic contacts to CNTs have been reported in the literature. Because of the Ohmic contacts, it is believed that the physics governing the transistor action is the bending of the bands by the applied gate voltage. Theoretical work [Leo02] to explain this behaviour has been presented in the literature. Results of such work, based on quantum transport calculations, are presented in figure 41. Panel (*a*) in the figure shows the calculated zero bias conductance as a function of the gate voltage. The device shows three regimes: in regime I the conductance is high, corresponding to the ON state of the transistor. In this regime, the bands are essentially straight (figure 41(*b*)) so that there is little scattering of electrons at the Fermi level. Since the conduction band

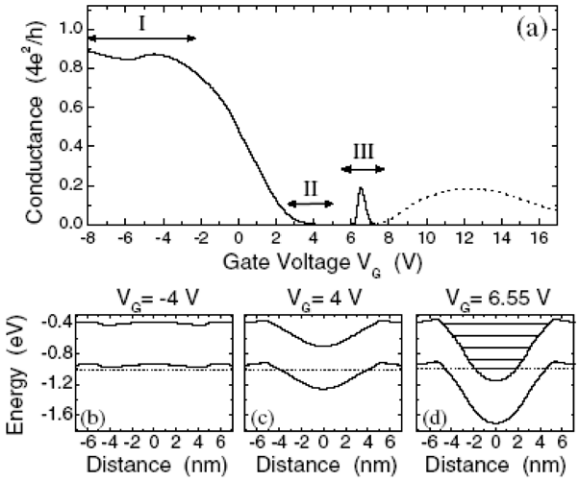


**Figure 41.** (*a*) The calculated zero-bias conductance of a nanotube FET. (*b–d*) Band bending associated with regimes I, II and III of panel (*a*).

is degenerate, the conductance in this regime saturates to a value close to two quanta of the conductance. As the gate voltage is increased, the conductance decreases sharply and the transistor enters the OFF regime. This regime is characterized by a large barrier in the middle of the CNT that blocks the electrons (there is a small leakage current due to the source–drain tunnelling). As the gate voltage is further increased, the channel is driven into inversion. While at micron-sized channels this inversion leads to a permanent turn-on of the conductance, for nanometre-sized channels the situation is quite different. In this case, the band bending creates an electrostatic quantum dot in the middle of the CNT, leading to the appearance of localized energy levels. Thus, the inversion regime in nanoscale CNT transistors consists of resonant tunnelling through these discrete levels, leading to a peak in the conductance in regime III. This regime is expected to have intriguing behaviour such as high frequency response and has yet to be explored experimentally.

The main conclusion of this section is that the behaviour of Ohmic CNT transistors is determined by changes in the band bending of the CNT in the channel region. As we will see in the next section, CNT transistors with Schottky contacts behave much differently.

*4.3.2. CNT transistors with Schottky contacts.* As we have discussed in section 3, CNT/Ti contacts are characterized by the presence of Schottky barriers. Normally, the current across such contacts is dominated by thermionic emission, where electrons must be thermally excited over the Schottky barrier. However, if the band bending near the contact is very sharp, electrons can tunnel across the sharp band bending, leading to a much increased current. This is precisely the effect that governs the operation of the Schottky Barrier CNT FETs, as illustrated in figure 42.

In figure 42(*a*), the band-bending is sketched for the OFF state of the transistor. At this gate voltage, the tunnelling length near the contact is long and the tunnelling current is small. Increasing the gate voltage as shown in figure 42(*b*) raises the bands in the middle of the CNT, leading to a much reduced tunnelling distance at the contacts and a larger current. The device operation is thus controlled by modulation of tunnelling at the contacts, a mechanism that is entirely different from the conventional transistors and the Ohmic contact CNT FETs.

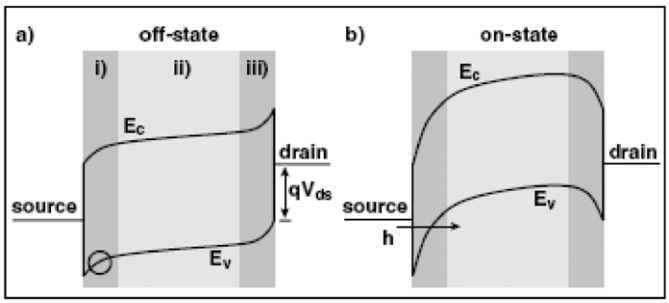


**Figure 42.** Band bending in a Schottky Barrier CNT FET, for two values of the gate voltage. From [Ape02].

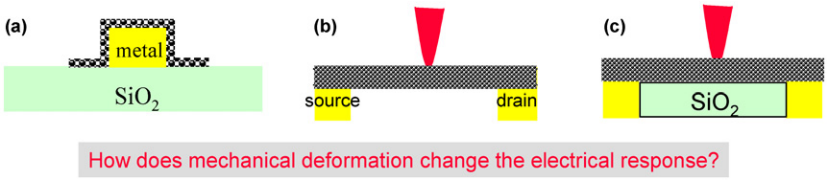


How does mechanical deformation change the electrical response?

**Figure 43.** Experiments involving electromechanical properties of nanotubes. (*a*) A nanotube bent around edges, as a result of the van der Waals interaction. (*b*) A nanotube is suspended between contacts. A gate voltage (not shown) pulls the nanotube down, which changes the conductance. Pushing the nanotube down with an AFM tip, which results in bond stretching, also deforms the suspended nanotube. (*c*) A nanotube lying on a hard substrate is deformed using an AFM tip, which significantly affects its cross section.

## 5. Electromechanical properties

The electrical response of nanostructures to mechanical deformation is relatively unexplored and is of both fundamental and applied interest. In nanotubes, mechanical deformations induce significant sigma–pi coupling, stretching and compression of bonds, all of which affect electronic properties and conductance. Potential applications of nanotubes in nanoelectromechanical systems (NEMS) are actuators, oscillators and electromechanical memory, which are being pursued by various groups [Bau99, Rue00, Saz04, Sti05]. In section 5.1, we discuss the change in the conductance of nanotubes under bending. In sections 5.2 and 5.3, we discuss the change in the bandgap under uniaxial strain and radial deformation, respectively. Two recent examples of devices based on electromechanical response are discussed in section 5.4.

### *5.1. Bent nanotubes*

Nanotubes are not structurally perfect in transport experiments. Interaction with metal contacts and substrate cause the nanotube to bend as shown in figure 43(*a*). This affects the flow of electrons from source to drain and alters device properties. The deformations along the circumference that accompany bending can be very asymmetric, where bonds in the concave side are stretched while bonds in the convex side are compressed. Modelling shows that transmission of nanotubes bent by 36° or more is 2–3 times smaller than the theoretical maximum in armchair and zigzag nanotubes [Leo05, Mai02, Nar99, Roc99]. An example of a bent (6,6) armchair nanotube is shown in figure 44(*a*), where the effect of the metal substrate

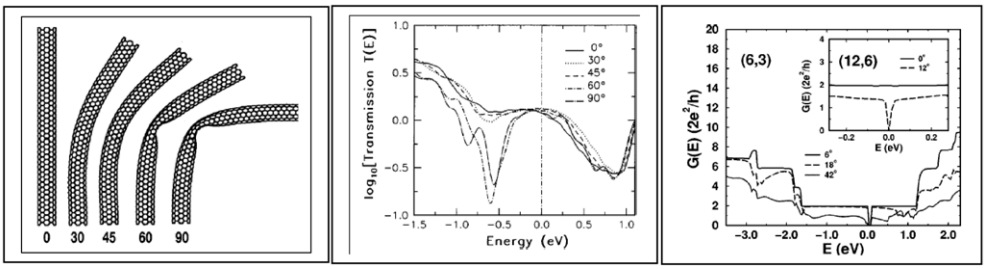


**Figure 44.** (*a*) A (6,6) armchair nanotube at various bending angles indicated at the bottom of the figure. (*b*) The transmission versus energy for various bending angles corresponding to (*a*). Source: [Roc99]. (*c*) Transmission versus energy of (6,3) and (12,6) chiral nanotubes at various bending angles. In comparison with the armchair and zigzag nanotubes, chiral nanotubes show a larger change in transmission at the Fermi energy even at small bending angles. From [Nar99].

is neglected. The corresponding transmission versus energy is shown in figure 44(*b*), which shows only a small decrease in transmission at the Fermi energy. Away from the Fermi energy at around $E \sim -0.5$ eV, the transmission is about ten times smaller because of the sigma–pi hybridization. In comparison to armchair and zigzag [Mai02] nanotubes, the transmission of chiral nanotubes decreases sharply at the Fermi energy to almost zero upon bending as shown in figure 44(*c*) [Nar99]. This is attributed to the low symmetry of chiral nanotubes. Based on the body of evidence from the modelling and experiments, it can be concluded that for the armchair and zigzag nanotubes the extra resistance due to bending is on the order of the quantum of conductance (12.9 kΩ). Chiral nanotubes, on the other hand, have a much larger resistance due to bending.

### 5.2. *Effects of uniaxial and torsional strain on electronic properties*

Nanotubes show a dramatic bandgap dependence on uniaxial and torsional strain [Hey97, Gar03, Kle01, Liu00, Mai02, Yan99, Yan00]. At the one extreme are the armchair nanotubes, which remain metallic under tensile strain due to the preservation of mirror symmetry under uniaxial strain. At the other extreme, the rate of change of the bandgap with strain is largest for zigzag nanotubes. In general, the rate of change of the bandgap with uniaxial strain, $d(\text{bandgap})/d(\text{strain})$, of any nanotube is given by (within the uniform $\pi$ orbital tight-binding approximation discussed in section 1)

$$\frac{d(\text{bandgap})}{d(\text{strain})} = \pm 3\gamma \cos(3\theta), \tag{5.2.1}$$

where $\theta$ is the chiral angle. The bandgap versus strain is shown for various chiralities in figure 45. For zigzag nanotubes, equation (5.2.1) gives a bandgap change of $3|\gamma|\sigma$ where $\sigma$ is the strain. This corresponds to a bandgap change of 81 meV at 1% strain in the zigzag nanotubes. As the chiral angle decreases, the absolute value of $d(\text{bandgap})/d(\text{strain})$ decreases and becomes zero for armchair nanotubes (chiral angle is 30°). The sign of $d(\text{bandgap})/d(\text{strain})$ has an interesting dependence on $(n - m)$ for a general $(n, m)$ nanotube. The slope is positive for $n - m = 3 * I + 1$ and negative for $n - m = 3 * I - 1$ that is, if $n - m = 3 * I + 1$, the bandgap increases for extension and decreases for compression. The above discussion surrounding equation (5.2.1) is valid only within the uniform $\pi$ orbital tight-binding approximation. There are small deviations when a four orbital model is used. The most notable deviation is for semi-metallic nanotubes (satisfying $n - m = 3 * I$), which

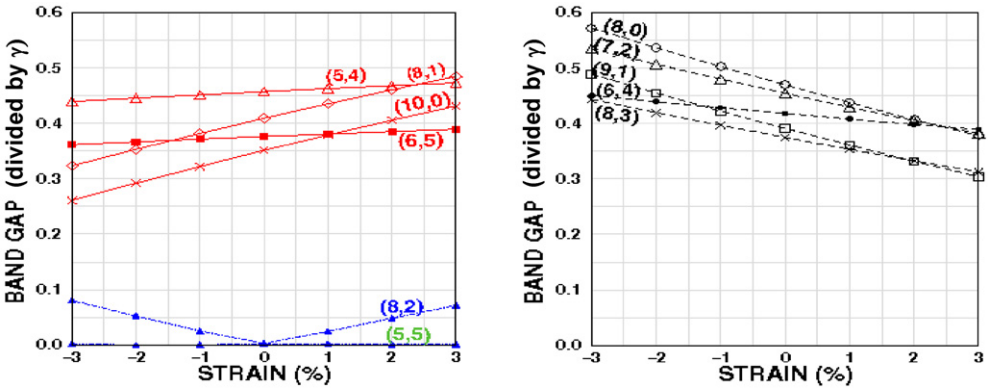


**Figure 45.** Bandgap versus uniaxial strain. (*a*) Nanotubes satisfying $n - m = 3 * I$ develop a bandgap except for the armchair nanotubes, which remain metallic with uniaxial strain. Nanotubes satisfying $n - m = 3 * I + 1$ have a positive slope of $d$(bandgap)/$d$(strain). (*b*) Nanotubes satisfying $n - m = 3 * I - 1$ have a negative slope. The magnitude of $d$(bandgap)/$d$(strain) decreases with the chiral angle. All results are within the $\pi$ orbital approximation with $\gamma \sim 2.77$ eV.

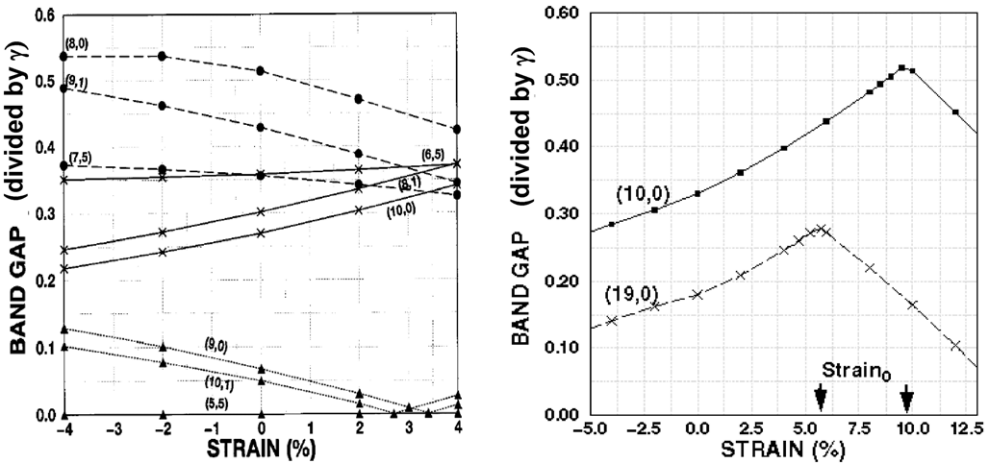


**Figure 46.** (*a*) Bandgap versus uniaxial strain calculated using a four orbital tight-binding model. The results confirm the findings of the $\pi$ orbital calculation shown in figure 45 except for semi-metallic tubes. Source: [Yan99]. (*b*) Bandgap versus uniaxial strain for large values of strain calculated within the $\pi$ orbital approximation. The important point here is that the bandgap change reverses sign at around 6% and 9.5% strain, for (19,0) and (10,0) nanotubes, respectively.

have a tiny curvature induced bandgap at zero strain. Stretching causes this bandgap to close, followed by a bandgap opening with increasing strain as shown in figure 46(*a*).

With increasing strain, a reversal of bandgap change occurs as shown in figure 46(*b*). The bandgap of both the (10,0) and (19,0) nanotubes increases with strain but begins to decrease after ∼6% and ∼9.5% strain, respectively. The reason for this is as follows. Consider the two lowest subbands with energy greater than zero. Because of the strain, the lowest subband increases in energy, but the second lowest subband decreases in energy. The reversal in the bandgap change corresponds to the crossover point between these two bands [Yan99].

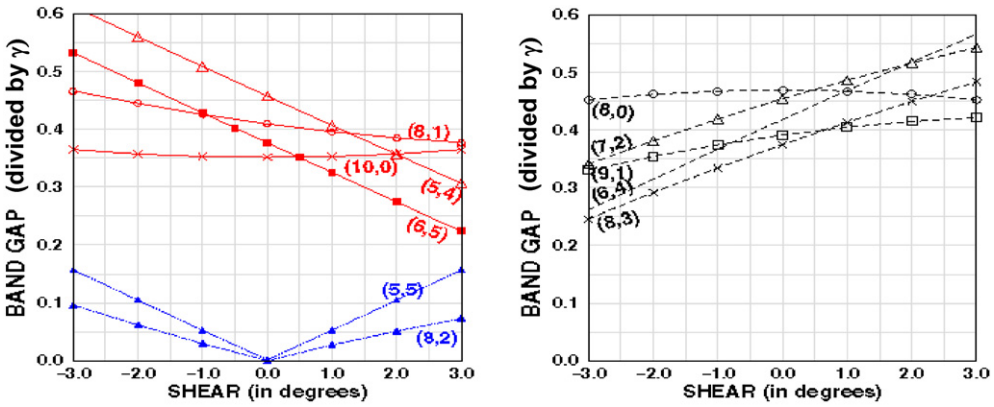


**Figure 47.** Bandgap change with torsional strain. (*a*) Armchair nanotubes develop the largest bandgap under torsional strain and zigzag tubes develop the smallest bandgap. $d$(bandgap)/$d$(strain) is negative for nanotubes satisfying $n - m = 3 * I + 1$. (*b*) $d$(bandgap)/$d$(strain) is positive for nanotubes satisfying $n - m = 3 * I - 1$. All calculations are within the $\pi$ orbital approximation with $\gamma \sim 2.77$ eV.

The bandgap change in the presence of torsional strain is quite the opposite of tensile strain (figure 47) [Yan99]. The bandgap change is largest for armchair nanotubes, with $d$(bandgap)/$d$(strain) being approximately $3|\gamma|$, independent of diameter (figure 47 (*a*)). The bandgap of armchair nanotubes changes by approximately 81 meV for 1% torsional strain. As the chiral angle decreases, the absolute value of $d$(bandgap)/$d$(strain) decreases and is smallest for the zigzag nanotubes (figure 47). The slope of change in the bandgap with torsional strain is negative for $n - m = 3 * I + 1$, and positive for $n - m = 3 * I - 1$ in contrast to the uniaxial case discussed above. Finally, small changes similar to the uniaxial strain case result from a four orbital treatment of semi-metallic nanotubes [Yan99].

There have been many experiments exploring the electromechanical response of nanotubes [Pau99, Pon99, Pur02, Bab03, Tom00, Saz04]. A remarkable experiment [Tom00] measured the change in the conductance of a nanotube suspended in a trench created in a SiO2 substrate (figure 48). The nanotube was deformed with an AFM tip as shown in figure 48(*c*), and the small bias conductance changed by two orders of magnitude upon deformation (figure 48(*d*)). Withdrawing the AFM tip resulted in the conductance returning to its undeformed value. There are two potential reasons for the change in conductance experimentally seen. The first reason is that the large local deformation under the AFM tip acts as a scattering centre. The second reason is that stretching of metallic nanotubes leads to a strain-induced bandgap as discussed above. A combination of the experimental and modelling work [Liu00, Mai02, Min03] showed that the change in conductance was due to a strain-induced bandgap discussed in this section. More importantly, these references also showed that the magnitude of the induced bandgap depends on the CNT chirality.

### *5.3. Effect of radial deformation on electronic properties*

Electronic properties of nanotubes change significantly upon radial deformation. Deformations of a nanotube lying on a hard substrate by an AFM tip as shown in figure 43(*c*) has been experimentally demonstrated in [Pau99] and [Gom04]. Such a deformation causes a large change in the cross section of the nanotube region under the AFM tip but the deformation is small away from the tip. Modelling has focused on the simpler case of change in the bandgap

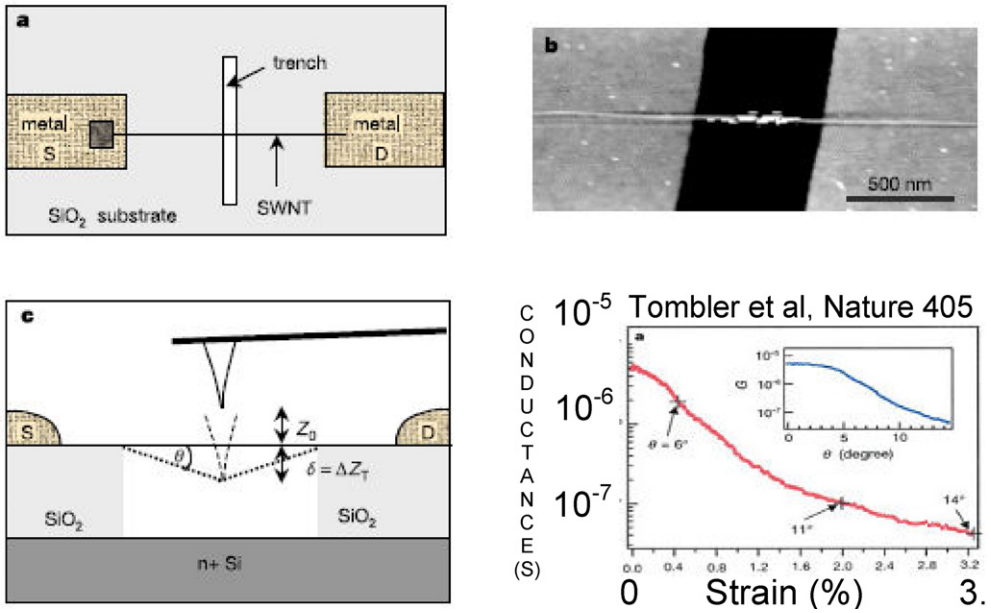


**Figure 48.** A SWNT suspended over a trench for electromechanical measurements. (*a*) Device viewed from above. The substrate has a trench that is about 500 nm in width and 175 nm in depth. The SWNT bridging a pair of metal electrodes (S and D refer to source and drain) is suspended over the trench. (*b*) An AFM image of the SWNT suspended over the trench. (*c*) Side view of (*a*) which shows the AFM tip pushing the nanotube down into the trench. (*d*) The experimentally measured conductance versus strain shows a two order of magnitude change in conductance. The diameter of the SWNT is ∼3 nm. From [Tom00].

under uniform radial deformation of infinitely long nanotubes, which nevertheless gives a useful insight [Gul02, Kil00, Lu03, Meh05, Par99].

The bandgap change in radial deformation is very sensitive to the details of the nanotube cross section. The cross section, in turn, depends on the nanotube-substrate and nanotube-tip interaction. An example of such a deformation is shown in figure 49(*a*), and is characterized by a parameter $d_{\mathrm{TB}}$ measuring the distance between the top and bottom of the nanotube. If perfect symmetry is maintained upon deformation, then an armchair nanotube does not develop a bandgap [Gul02, Kil00, Lu03, Meh05, Par99] as shown in figure 49(*b*). A change from the perfect symmetry causes a bandgap that can be quite large but becomes zero with an increase in deformation, irrespective of the symmetry as shown in figure 49. Depending on the symmetry, the bandgap can oscillate with decreasing $d_{\mathrm{TB}}$ as shown by the two humps in figure 49(*c*). The increase in bandgap with deformation may also be monotonic before bandgap closing as shown in figure 49(*d*). The opening of a bandgap at large $d_{\mathrm{TB}}$ in figure 49 is because of interactions between $\pi$ orbitals at the top and bottom of the nanotube. With decreasing $d_{\mathrm{TB}}$, the $\sigma$–$\pi$ interactions at nanotube edges become important (figure 49(*a*)) and are responsible for the bandgap oscillations.

In the case of undeformed semi-metallic zigzag nanotubes satisfying $n - m = 3 * I$, there is a small curvature induced bandgap. This bandgap is about 100 meV for a (9,0) nanotube. Upon radial deformation, [Par99] found that the bandgap initially increases with the decrease in $d_{\mathrm{TB}}$. The bandgap becomes zero for $d_{\mathrm{TB}} < 6$ Å, and the nanotube remains metallic with further deformation (figure 50).

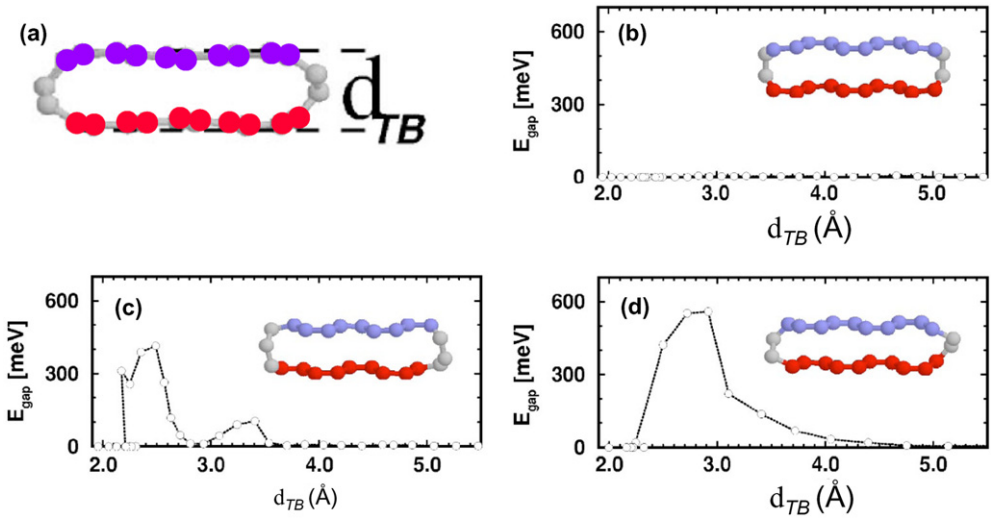


**Figure 49.** Bandgap of a (6,6) armchair nanotube as a function of $d_{\mathrm{TB}}$ for different initial conditions. (*a*) $d_{\mathrm{TB}}$ is the distance between the top and bottom of the nanotube. (*b*) When perfect symmetry is maintained a bandgap does not develop. (*c*) The bandgap oscillates as a function of $d_{\mathrm{TB}}$. (*d*) A different initial condition shows that the bandgap increases monotonically with $d_{\mathrm{TB}}$ and approaches 600 meV. When $d_{\mathrm{TB}}$ becomes smaller than approximately 2.2 Å, the bandgap becomes zero for all cases. From [Meh05].

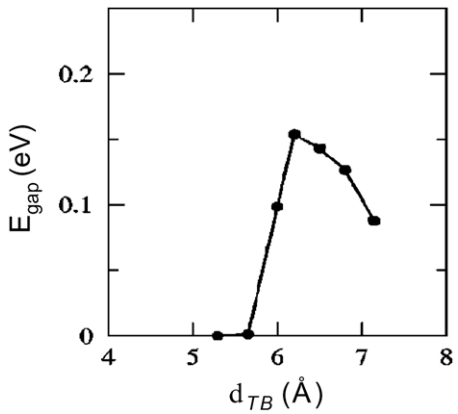


**Figure 50.** Bandgap of a (9,0) zigzag nanotube as a function of $d_{\mathrm{TB}}$. The bandgap of the undeformed nanotube at $d_{\mathrm{TB}} \sim 7.2$ Å is induced by curvature. As a result of the deformation, the bandgap initially increases before becoming zero at $d_{\mathrm{TB}} \sim 5.7$ Å. From [Par99].

### *5.4. Devices*

*Electromechanical oscillator.* An electromechanical oscillator based on a nanotube has been experimentally demonstrated in [Saz04]. The device consists of a three terminal transistor-type device with a nanotube forming the channel (figure 51). The nanotube is suspended in a channel between the source and drain and is capacitively coupled to the gate terminal. Applying an ac voltage to the gate causes the nanotube to mechanically oscillate. When the applied ac frequency matches the resonant frequency of the nanotube, the amplitude of the mechanical

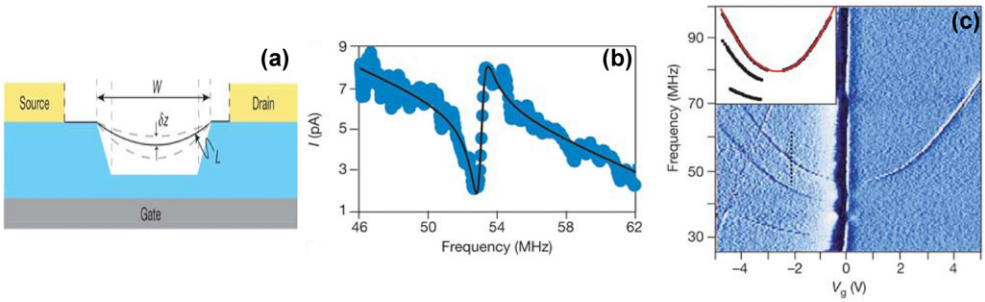


**Figure 51.** (*a*) Image of a suspended nanotube bridging a trench. The metal electrodes are shown in yellow. A dc gate voltage modulates the tension in the nanotube and an ac gate voltage causes mechanical oscillations shown by $\delta z$. When the frequency of the ac voltage matches the natural resonant frequency of the nanotube, $\delta z$ becomes large. (*b*) The experimentally measured source–drain current as a function of the frequency of ac voltage applied to the gate, at a dc gate voltage of 2.2 V. The solid line is a lorenzian fit and the resonant frequency is 55 MHz as can be seen in the plot. (*c*) The experimentally measured resonant frequency (*y*-axis) as a function of change in the tension of the nanotube, which is controlled by changing the dc gate voltage (*x*-axis). From [Saz04].

oscillation becomes large. The mechanical oscillations cause a change in the capacitance between the nanotube and gate. The induced ac charge in the nanotube has two components, one due to the change in capacitance between the nanotube and gate ($C_g$) and the other due to the change in gate voltage ($V_g$),

$$\delta q = C_g \delta V_g + \delta C_g V_g. \tag{5.4.1}$$

The ac current in the nanotube has two components which correspond to the two terms of (5.4.1). Of these, only the component corresponding to the second term depends on mechanical oscillations of the nanotube because $C_g$ changes as a function of the nanotube-gate distance. Thus the ac current magnitude due to the second term is largest at resonance when the amplitude of the mechanical oscillation is largest. Overall, the device in figure 51 has an enhanced source–drain ac conductance when the driving frequency of the gate matches the resonant frequency of the nanotube for mechanical oscillations. A typical experimental result is shown in figure 51(*b*), where the ac component of source–drain current has a maximum at a frequency of 55 MHz.

Changing the length and diameter of the nanotube, which changes the mass of the oscillator, alters the resonant frequency. Also, tuning the tension in the nanotube by changing the dc gate voltage can be used to tune the resonant frequency. Figure 51(*c*) shows the experimentally observed change in resonant frequency as a function of dc gate voltage. Nanoscale oscillators can potentially be used in applications such as cell phones and sensors to detect ultra small masses approaching that of a single atom [Saz04a].

*Nanotube memory.* Another exciting application of the CNT electromechanical response has been the development of a new CNT memory [Rue00, Sti05]. This memory uses a silicon platform while nanotubes form the channel to store information (figure 52). The channel consists of aligned nanotubes lying between a source and drain (interconnects in figure 52(*a*)) and the channel is capacitively coupled to a gate electrode. The nanotube array is suspended either with or without contact with the electrode depending on the voltage of the electrode. Binary 0 and 1 states are determined by whether or not the nanotube fabric makes contact with the electrode. Binary 0 is represented by the state where there is a ∼13 nm gap between the

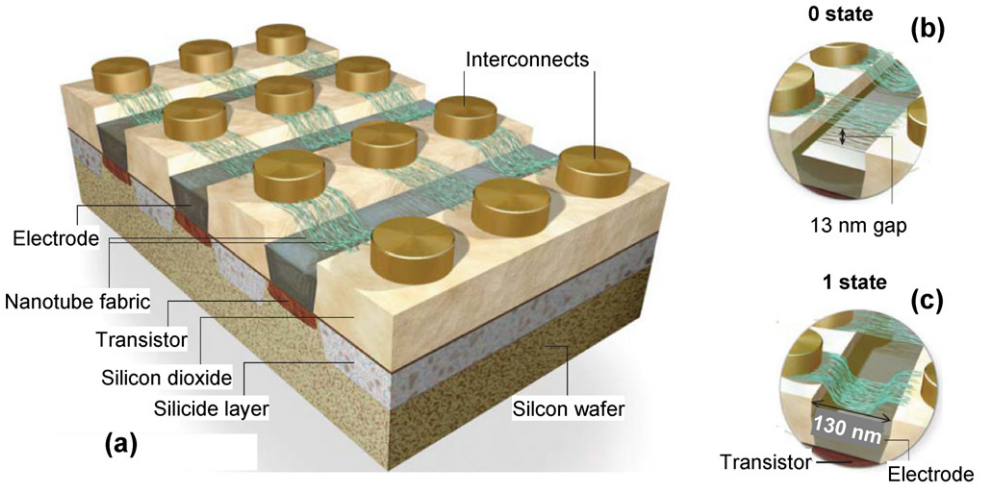


**Figure 52.** RAM made with a nanotube fabric. (*a*) The nanotube memory array. The memory density and speed is comparable to that of DRAM. (*b*) A binary 0 state corresponds to the nanotube suspended and not making contact with the electrode. (*c*) A binary 1 state corresponds to the nanotube making contact with the electrode. The length of the suspended nanotubes is 130 nm. From [Sti05].

nanotube fabric and electrode as shown in figure 52(*b*). The application of a voltage to the electrode pulls the nanotube fabric down such that it makes contact with the electrode and this state represents binary 1 (figure 52(*c*)). The binary 1 state is read by detecting a flow of current from the interconnect to the electrode. This current is non-zero only when the nanotubes make contact with the electrode. An advantage of this memory is that it is both non-volatile and fast. Once a 1 state is written, the voltage applied to the electrode can be removed; the van der Waals interactions between the nanotubes and the electrode hold the memory in the 1 state for a very long time. The access time of this non-volatile nanotube random access memory (RAM) is comparable to that of the conventional DRAM/SRAM [Rue00, Sti05].

## 6. Field emission

### *6.1. Introduction*

Prototype devices using the superior field emission properties of nanotubes have been demonstrated. These devices include x-ray tubes [Sug01], scanning x-ray sources [Zha05], flat panel displays [Cho99a], and lamps [Cro04]. There are many reasons for the excellent field emission properties of CNTs. The first reason is the inertness and temperature stability of the CNT tips for long periods of operation compared with the metal and diamond tips; due to their covalent bonding structure, nanotubes do not suffer from electromigration. The second reason is a low threshold voltage for cold field emission from nanotube tips. Other advantages are low temperature of operation, ultra small response times, low power and small size. The reason for the low threshold voltage follows from the conventional Fowler–Nordheim (FN) model, which relates the field emission current ($I$) to the applied voltage ($V$) and work function ($\phi$) of the field emitter by

$$I = aV^2 \exp\left(-\frac{b\phi^{1.5}}{\beta V}\right), \tag{6.1.1}$$

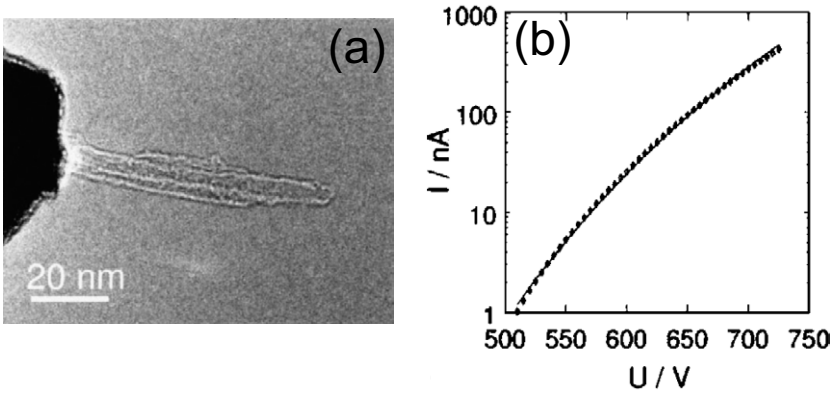


**Figure 53.** (*a*) Transmission electron microscope image of a nanotube on a tungsten tip. (*b*) Field emission current as a function of the applied bias. Note the good match to the FN model (——). From [Jon04].

where $\beta$, which depends on the geometry of the tip is called the field enhancement factor. The physical reason for the low operating voltage of the field emission is the large aspect ratio (height to diameter) of nanotubes, which results in a large $\beta$. A large value of $\beta$ implies that the electric field near the tip is large, and hence electrons can easily tunnel from the field emission tip.

An important question is the validity of the traditional FN model to describe field emission from nanotube tips. The unique bandstructure with the van Hove singularities in the density of states and localized/quasi-localized states at the tip may necessitate the need for a new model to describe field emission from nanotubes. While both the experiments and theory have explored this topic, there is no clear conclusion. However, most experiments show that the *total* field emission current as a function of bias is quite consistent with the FN model in SWNTs [Rin95, Jon04], ropes [Lov00, Bon02], films [Bon02, Che95, Hee95] and patterned films [Wan98]. A field emission tip consisting of a single MWNT with a radius of about 5 nm, attached to a tungsten tip is shown in figure 53(*a*) [Jon04]. Here, one can clearly see the large aspect ratio (length to diameter) achieved experimentally. The current–voltage characteristics are reasonably consistent with the FN model over a current window spanning more than two orders of magnitude (figure 53(*b*)). Deviations from the FN model for the total current have been observed in specific samples because of adsorbates and possibly the quantized energy levels in the tip. This topic will be discussed in section 6.2.

The total energy distribution (TED) of electrons is an interesting quantity as it gives information on the electronic structure of the nanotube tip. In contrast to the total current, both the experiments and modelling show that the TED of the current (field emission current spectrum as a function of energy) can differ from the FN behaviour. While experiments on a single nanotube showed reasonable agreement with the FN model [Jon04], experiments have shown deviations in the TED in samples consisting of a bundle of SWNTs [Lov00]. Localized states in the tip cause a significant change in density of states and the emitted current has signatures of the van Hove singularities in the nanotube (see figure 7) shown by modelling by [Car97, Vit99, Ade00, Ana00].

The TED corresponding to the experiment discussed in figure 53 is shown in figure 54(*a*). The TED reasonably follows the FN model over a large energy window. In contrast, field emission from a SWNT bundle shows a TED that is different from the FN model. Figure 54(*b*) compares the experimental results of TED from a SWNT rope with the FN model [Lov00].

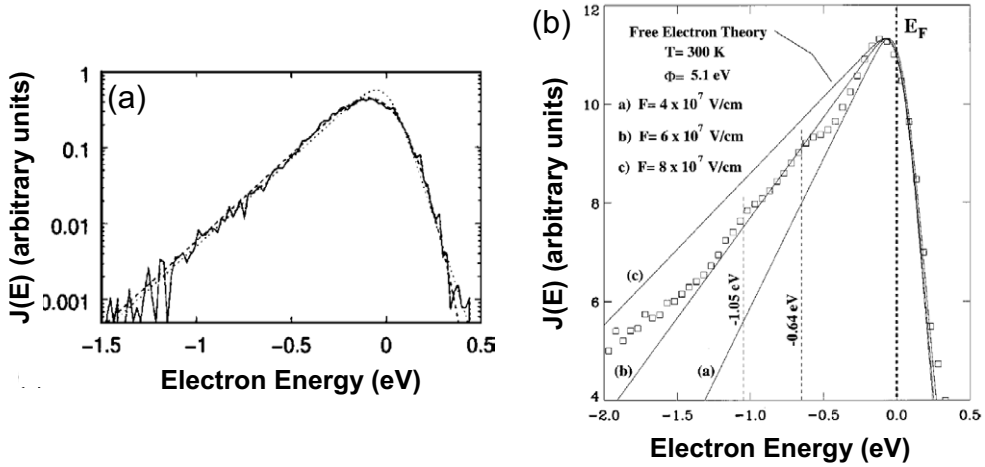


**Figure 54.** (*a*) TED of emitted current corresponding to the single nanotube in figure 53, at room temperature, applied voltage of 552.8 V and an emitted current of 11 nA. Source:c̃iteJon04. (*b*) Log of TED versus energy for electron field emitted from a SWNT rope. Solid lines show the predictions of the FN model for three different values of the electric field $F$. The Fermi energy ($E_F$) and features representing deviations from the FN model at energies of $-0.64$ and $-1.05$ eV are marked by dotted lines. From [Lov00].

While the net current agrees with the FN model, noticeable deviations from the FN model are seen in the TED around the Fermi energy and at energies $-0.6$ and $-1.05$ eV below the Fermi energy. The deviations around the Fermi energy are attributed to the dangling bond states in open nanotubes [Vit99], while the deviations at the other two energies were found to correlate with the van Hove singularities in one-dimensional density of states due to subband openings.

### *6.2. Role of adsorbates and the role of nanotube density in field emission from an array*

Experiments have shown a significant deviation from the FN model in the presence of adsorbates. Adsorbates can change the threshold voltage due to a change in the work function in equation (6.1.1). In addition, there can also be a change in the overall slope of the current–voltage characteristics. Both features were seen in an experiment that measured the current–voltage characteristics in a controlled environment, with and without adsorbates [Dea00]. In this controlled experiment, adsorbates were intentionally introduced by exposing the sample to $H_20$ under a partial pressure of $10^{-7}$ Torr for 5 min. Adsorbates cause a negative shift in the threshold voltage and also cause current saturation in a large voltage window from 1600 to 2200 V. However, either heating the tip to 900 K under field emission conditions or large applied voltages led to regular field emission behaviour without current saturation because of adsorbate desorbtion. Note that in figure 55(*a*), the current with adsorbates saturates at higher voltages before beginning to increase again at 2300 V, when the data becomes similar to the clean sample. A downward sweep after such large applied voltages showed current–voltage characteristics of a clean sample. This remarkable experiment also showed that adsorbates change the shape of the field emission pattern (figure 55(*b*)). The field emission pattern in a clean sample is shown in panel (i). Introducing water causes a significant deviation in the pattern as shown in panel (ii). The reverse sweep after applying a voltage of 2300 V matches the pattern with a clean tip due to desorbtion of the adsorbate as shown in panel (iii).

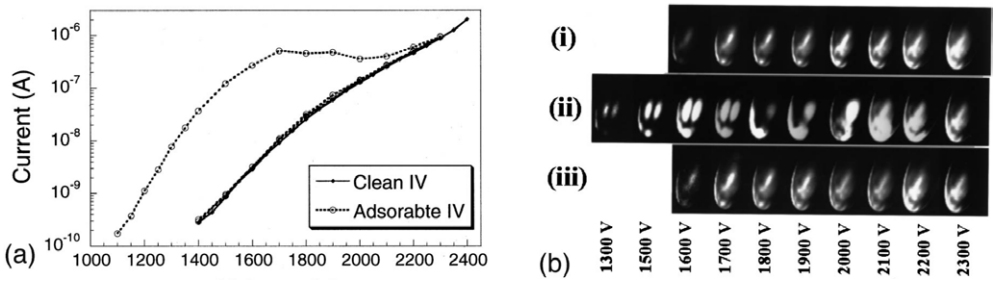


**Figure 55.** (*a*) Current–voltage characteristic of a single SWNT with and without adsorbates. (*b*) The field emission pattern of a clean SWNT is stable over the voltage sweep (i) but the pattern of the same nanotube with an adsorbate changes during the current–voltage sweep concurrent with the onset of current saturation (ii). At 2300 V, the effects of the adsorbates disappear, resulting in a clean nanotube field emission pattern. During the downward $I$–$V$ sweep, images (iii) match the clean SWNT shown in (i). From [Dea00].

We have so far discussed the field emission from a single nanotube or a single bundle. Applications in display devices will however involve CNT films or arrays because of the need for field emission over large areas. To be competitive with conventional field emitters, nanotube films should exhibit uniformity with an areal density larger than $10^6$ emitters cm$^{-2}$ and current densities of 80 $\mu$A cm$^{-2}$ [Nil00]. It has recently been shown that field emission from nanotube films is dominated by a small percentage of nanotubes with a large length to diameter ratio, which corresponds to a large field amplification factor $\beta$. The field emission current and the threshold voltage also depend on the areal density of nanotubes because of electrostatic screening. Figure 56 shows the SEM images (left) of patterned nanotube films of low, medium and high areal densities. Clearly, the sample with medium density provides the best image of the emission pattern. This is because the low density pattern has very few efficient emitters while the high density pattern suffers from electrostatic screening due to the neighbouring nanotubes, which diminishes the field enhancement factor $\beta$. Simulations also show that the field penetration diminishes as nanotubes are packed more densely and this affects both $\beta$ and the current [Nil00]. Figure 56(*h*) shows the field penetration in an array consisting of nanotubes 1 $\mu$m in length and a radius of 2 nm. Clearly the penetration is poor when the spacing between tubes is 0.5 $\mu$m (bottom) as opposed to 4 $\mu$m (top). The corresponding field enhancement factor also increases with the increase in nanotube spacing as shown in figure 56(*i*). The simulated current density clearly is peaked at nanotube spacings comparable to 2 $\mu$m as shown in figure 56(*j*), signifying again an interplay between the areal density and the field amplification factor $\beta$ in determining the current.

### *6.3. Devices*

*Field emission display.* Displays using the superior field emission properties of CNTs have been demonstrated by a number of groups. Figure 57 shows a multicoloured display demonstrated in [Cho99a]. The display consists of CNT tips on a patterned metal substrate as shown in figure 57(*a*). The CNT bundles are firmly attached to the metal electrode and are quite uniform over the 4.5 inch display (figure 57(*c*)). The nanotubes were not grown vertically from the substrate, but were mixed with an organic nitrocellulose to form a paste and then squeezed through a wire mesh to force alignment of nanotubes perpendicular to the metal as shown in figure 57(*b*). The density of nanotubes obtained is about $5 \times 10^6$–$10^7$ emitters cm$^{-2}$, which is about one hundred times larger than the density of microtips in the conventional Spindt-type

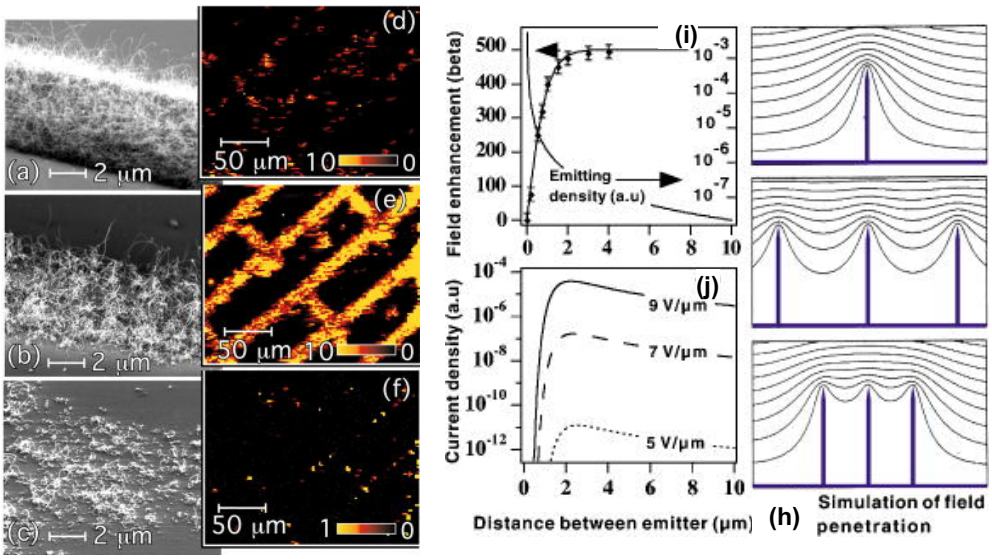


**Figure 56.** SEM images of patterned CNT films showing regions of (*a*) high, (*b*) medium and (*c*) low density, with the corresponding field emission maps of current density (*d*)–(*f*). The colour scale corresponds to 0–10 $\mu$A/pixel for images (*d*) and (*e*); and to 0–1 $\mu$A/pixel in image (*f*). (*h*) Simulation of equipotential lines of the electrostatic field for tubes of 1 $\mu$m in height and with a radius of 2 nm, for distances between tubes of 4, 1 and 0.5 $\mu$m, (i) Field enhancement factor and emitting density, and (*j*) current density, as a function of the distance between nanotube emitters. From [Nil00].

field emission displays. Since the initial work of [Cho99a], nanotube-based displays have become an important area of research and development, and Samsung demonstrated a 38 in colour television in 2003.

*X-ray tubes and spectrometers.* X-ray sources have many medical and industrial applications, in addition to their use as a spectroscopy tool in materials science. In conventional x-rays tubes, thermionically emitted electrons from a heated metal filament are accelerated and then strike a metal target, which releases x-rays. The high power consumption and small response times of thermionic sources makes x-ray generation using cold field emission attractive. Also, the high temperatures of thermionic sources place limitations on both the size and lifetime of x-ray tubes. Ultra sharp metal field emission tips obtained by micromachining have suffered from problems related to mechanical and thermal stability due to arcing and cation sputtering [Sug01, Yue02]. Similarly to the field emission displays, the advantage of the cold field emission from CNTs offers a potential for building smaller, portable, low power, long lifetime, x-ray tubes for various applications. CNTs overcome many problems associated with metal field emission tips because they are mechanically strong and can withstand higher temperatures.

Many applications of x-ray tubes require currents in the range of 50–500 mA cm$^{-2}$. Obtaining such high stable current densities over macroscopic areas using nanotubes has been challenging. Recently, however, current densities as large as 1 A cm$^{-2}$ have been obtained [Yue02, Sar05] though their stability over long periods of operation has not been determined. CNT x-ray tubes have been demonstrated as being capable of imaging circuit boards [Sug01] and a model of a human hand [Yue02]. More recently, a compact multibeam nanotube x-ray source capable of three-dimensional imaging (two dimensional frames at various angles) has

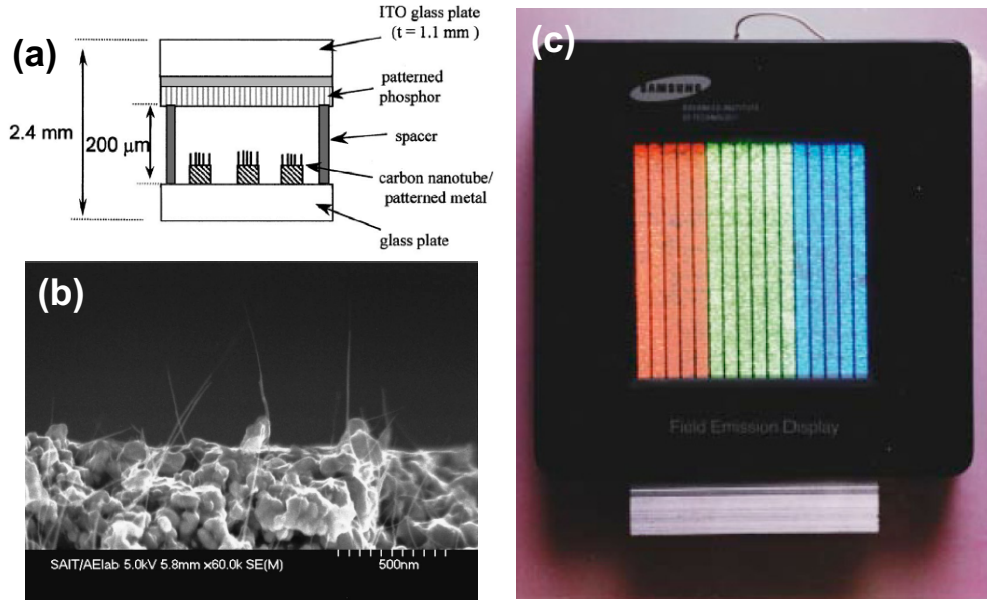


**Figure 57.** (*a*) Picture representing the set-up of a field emission display. CNTs are deposited on a patterned metal substrate. Field emitted electrons hit the phosphor screen and cause light emission in a colour that depends on the chemical compound on the phosphor screen. (*b*) SEM image of nanotube bundles projecting from the metal electrode. (*c*) A sealed CNT field emission display emitting light in three different colours. The dimension of the display is 4.5 in. From [Cho99a].

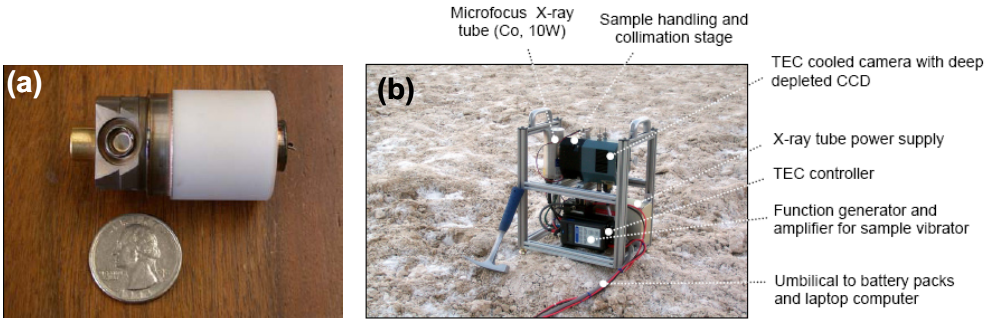


**Figure 58.** (*a*) A miniature field emission x-ray tube made of a 2 mm diameter MWNT cathode. Source: [Sar04] (*b*) CheMin, a portable x-ray spectrometer, with a geologist's hammer for scale. From [Sar05].

been demonstrated [Zha05]. The operation voltage of these x-ray tubes is in the 15–50 kV range, which is comparable to conventional sources. Another recent demonstration has been the x-ray tubes for spectroscopy applications using a CNT field emission source (figure 58(*a*)). This x-ray tube uses only 1.5–3 W and operates on batteries [Sar04]. Using such a small x-ray tube, a field deployable x-ray spectrometer called CheMin that weighs only 15 kg has been built [Sar05]. CheMin has been chosen to be a scientific instrument (figure 58(*b*)) to be flown as a part of the 2009 Mars Science Laboratory mission and will perform mineralogy experiments on the surface of Mars.

## 7. Opto-electronic devices

### *7.1. Introduction*

From the discussion in the previous sections, it is clear that much work has been done to fabricate and understand electronic devices made with CNTs. An area of research that is still in its infancy is that of opto-electronics with CNTs. There are several reasons why CNTs are interesting materials for opto-electronics. An important characteristic of opto-electronic materials is the presence of a direct bandgap, which allows electronic transitions between the valence and conduction band to proceed without the intervention of phonons. As the bandstructures of figure 5 indicate, CNTs are unique materials in this aspect because all of the bands have a direct bandgap. Thus, for a single CNT, there are multiple bands that can participate in opto-electronic events, spanning a wide range of energies. By combining multiple CNTs of different bands gaps, it should be possible to obtain a continuous response over a broad spectral range.

A problem that affects traditional bulk materials is the presence of defects, which lead to non-radiative processes that can significantly reduce the device efficiency. CNTs, with their low defect density, should thus be less sensitive to this problem. A further advantage of CNTs is related to the temperature dependence of the device performance. For a three-dimensional semiconductor, the carrier density peaks slightly above the band edge, because the density of states vanishes at the band edge. Varying the temperature leads to a change in the position of the peak and thus affects the device properties. For CNTs, however, the density of states has a singularity at the band edge and the carrier density always peaks at the band edge.

At the time of writing of this review, experimental and theoretical works on the opto-electronic properties of CNTs are just starting to emerge. Since there are two distinct areas in opto-electronics, photoconductivity and electro-luminescence, we discuss each of these separately.

### *7.2. Photoconductivity*

In general, simply illuminating a material will not lead to a net electronic current; the material symmetry has to be broken in order to create electron flow in a particular direction. Perhaps the simplest device that works in this manner is the p–n junction, which is at the heart of many opto-electronic devices such as solar cells. Figure 59 shows the calculated self-consistent band bending for such a CNT p–n junction. Clearly, the potential step at the junction breaks the spatial symmetry. Upon illumination of this device with photons of energy $h\omega$, electrons at energy E are excited to energy $E+h\omega$. The figure shows three allowable excitation processes in the p–n junction. Path 1 shows the excitation of an electron from the valence to the conduction band by the absorption of a photon of energy larger than the bandgap. Processes 2 and 3 show photon-assisted tunnelling processes when the photon energy is less than the bandgap.

Calculations of the photocurrent as a function of the incoming photon energy are shown in figure 60. The photoresponse shows multiple peaks due to the multiple direct bandgaps of the CNT. Each of the peaks has a maximum near the photon energy that corresponds to the bandgap of each of the bands. The low energy tail corresponds to photon-assisted tunnelling processes.

Experimental evidence for photo-induced currents in CNT devices has recently been reported, using lasers to illuminate individual nanotubes. Figure 61 shows the measured photocurrent across a single CNT connecting two electrodes when illuminated with a Ti : sapphire laser. The photocurrent shows a peak with photon energy, similar to the calculations indicated in figure 60. A particularly interesting aspect of the photoconductivity

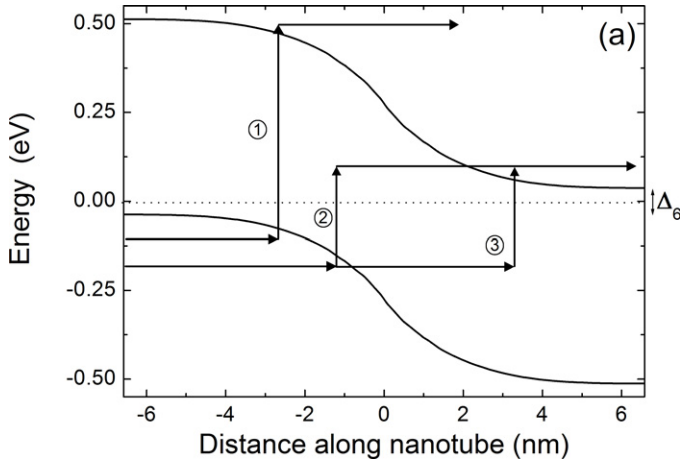


**Figure 59.** Calculated self-consistent band bending for a CNT p–n junction and the associated electronic transitions due to photon absorption. From [Ste04].

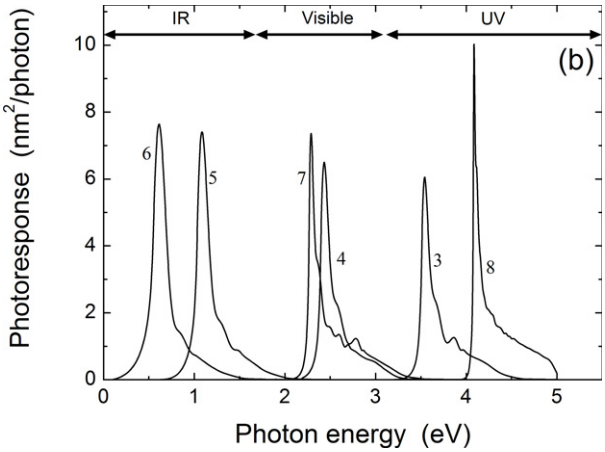


**Figure 60.** Calculated photoresponse of a CNT p–n junction to incoming light. Each of the peaks corresponds to a different band of the CNT, labelled with the value of the angular momentum. From [Ste04].

is the sensitivity of the photoresponse to the polarization of the incoming light. This sensitivity can be understood from symmetry considerations. Electron–photon interactions can be described with the Hamiltonian

$$H_{\text{el–ph}} = \frac{e}{m} A \cdot p, \tag{7.2.1}$$

where $A$ is the magnetic vector potential of the incoming radiation and $p$ is the electron momentum. For a zigzag CNT, the Hamiltonian matrix elements can be written as

$$H_{\text{el–ph}} = \begin{cases} \dfrac{e}{m} A\langle z', J|p_z|z, K\rangle & \text{parallel polarization} \\ \dfrac{e}{m} A\langle z', J|p_\phi|z, K\rangle & \text{perpendicular polarization,} \end{cases} \tag{7.2.2}$$

where $p_z$ and $p_\phi$ are the momentum operators in the axial and circumferential directions, respectively, and $|z, J\rangle$ represents the wavefunction of a CNT 'ring' at position $z$ along the

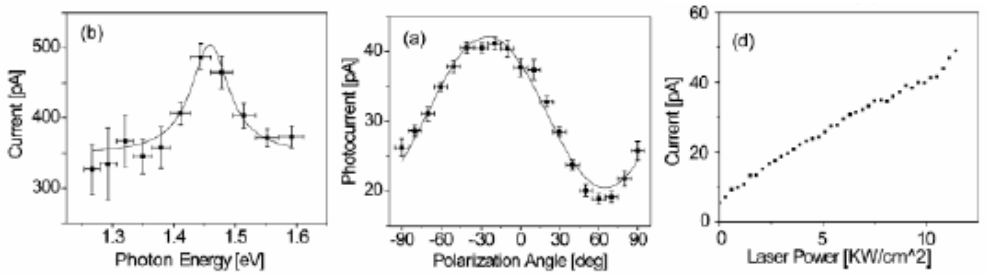


**Figure 61.** The left panel shows the measured photocurrent across a single CNT when illuminated with a Ti : sapphire laser, as a function of photon energy. The middle panel indicates photocurrent as a function of the polarization angle, while the right panel shows the linear dependence of the photocurrent on laser power. From [Fre03].

tube, for band $J$. From equation (7.2.2), it can be seen that in the case of parallel polarization, the momentum operator $p_z = i\nabla_z$ will only affect the $z$ dependence of the ring wavefunction and will not change the band indices. Thus, the matrix elements will be non-zero only when $J = K$. For perpendicular polarization, $p_\phi$ will increase the angular momentum by one unit to $K+1$, leading to the condition $J = K+1$. In the experiments, changing the polarization of the incoming laser light at fixed photon energy allows a probe of these selection rules, as shown in figure 61. Studies of the dependence of the photocurrent on the incoming laser power shows a linear behaviour, as shown in figure 61. These initial experiments and theoretical calculations clearly indicate that photocurrents can be generated in nanotube devices.

### *7.3. Electroluminescence*

Electroluminescence is the process by which current injection causes electron/hole recombination and photon emission. In conventional devices such as light emitting diodes, the simultaneous presence of electrons and holes in the same spatial region is achieved by operating a p–n junction in forward bias, thereby injecting electrons in the p region where they recombine with holes. In nanotube FETs, one can take advantage of the gate modulation of the contacts and the band bending to simultaneously inject electrons and holes in the nanotube. Thus, in CNT devices doping is not required to observe electroluminescence. The situation is illustrated in figure 62 which shows a sketch of the band bending along a semiconducting CNT making Schottky contact with the source and drain. Because of the relatively sharp band bending near the contacts, electrons (holes) from the drain (source) can tunnel into the CNT, and these simultaneous processes lead to recombination in the CNT. The resultant light emission is shown in figure 63. A particularly striking aspect of this device operation is that the spatial region where recombination occurs can be moved by changing the gate voltage as shown in figure 64.

It is quite clear that CNTs present many opportunities for electroluminescence, from fundamental science to more applied perspectives. More experimental and theoretical work is required to develop a detailed understanding of their unique properties.

## 8. Conclusions

In this paper, we reviewed the physics of CNT devices and illustrated their differences in comparison with the traditional bulk devices. After a brief introduction to CNTs,

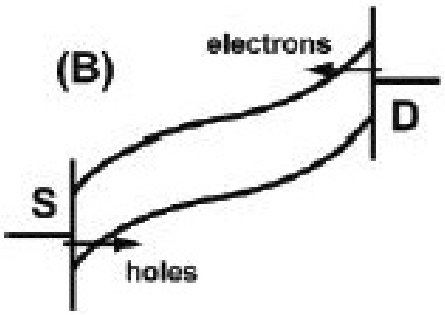


**Figure 62.** Sketch of band bending in CNT device for electroluminescence. Horizontal lines indicate the position of drain and source Fermi levels. From [Fre04].

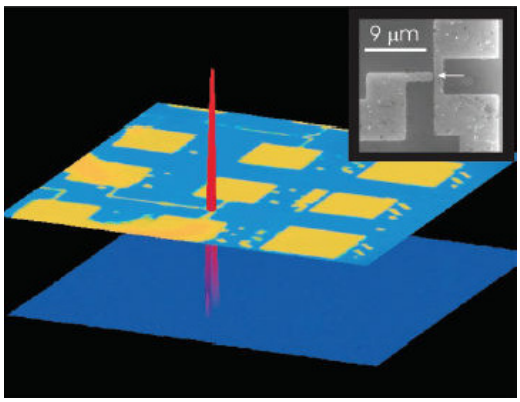


**Figure 63.** Optical emission from a CNT, captured by an IR camera. From [Mis03].

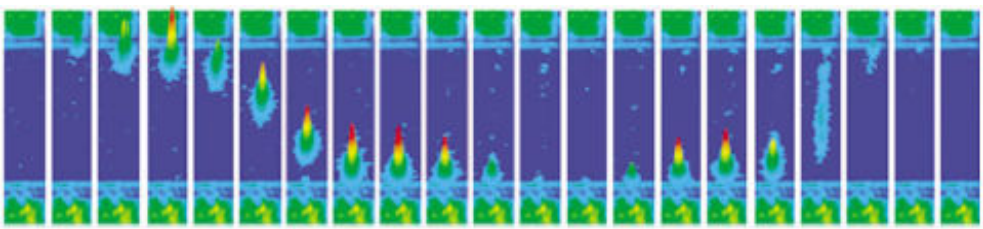

**Figure 64.** Light emission from a CNT FET during a gate voltage sweep. The gate voltage controls the band bending in the CNT and thus the location of the electron–hole recombination region. From [Fre04a].

we discussed metallic wires, metal-nanotube contacts, semiconducting electronic devices, electromechanical behaviour, field emission and optoelectronic devices.

The various sections included a description of the physics involved and a description of the prototype devices. The devices discussed fall into two categories. The first category consists of devices where the control of diameter and/or the chirality of an individual nanotube lying between contacts is necessary. Examples of these devices are single nanotube interconnects, diodes, transistors, light emitting diodes and electromechanical switches. Simple functional units such as logic gates and oscillators based on three nanotube transistors have been

demonstrated [Bac01, Der01]. The second category involves devices with many nanotubes between contacts, without the need for precise control over diameter and chirality of individual nanotubes. Examples discussed were field emission display, x-ray tubes and an electro-mechanical memory.

There are many challenges and opportunities, both for experiment and theory, which were not addressed in this review. We highlight a few here:

*Assembly.* From an applications perspective, control of individual nanostructures offers an enormous potential in terms of building the future generation of devices. However, it has proved very challenging from a fabrication viewpoint to create functional units consisting of even a few nanodevices. Both the control of chirality and the ability to place nanotubes at desired locations are topics of active research with many interesting problems and challenges, and advances will be critical to the success of CNT devices.

*Sensors.* An application of CNTs not discussed in this review but presenting much promise is sensors. Individual CNT field effect transistors have been used as chemical sensors to detect nitrogen dioxide and ammonia [Kon00] and to detect the controlled attachment of the redox enzyme glucose oxidase [Bes03]. Chemiresistors based on a network of CNTs lying on interdigitated gold electrodes have been used to detect various gases such as $NO_2$, nitrotoluene and $NH_3$ [Li04]. DNA sensors based on a macroscopically large nanoelectrode array of vertically aligned CNTs have been demonstrated [Li04a]. From a theoretical perspective, much work is needed to understand the role of analytes on nanotube electronic structure and transport.

*Time-dependent transport.* While much work has been done to understand the dc properties of electronic transport in CNTs, the time-dependent transport properties are relatively unexplored, despite their importance in device applications. Initial experiments have looked at the high-frequency behaviour of CNT transistors [Yu05], and we are aware of one theoretical work addressing the ac conductance [Rol00]. Much more work is needed in this area to perform high-frequency measurements and to develop theories and modelling approaches.

*Polymer composites.* The use of nanotubes to improve electrical and mechanical properties of polymers has also been an active topic of research. It has been found that the conductivity of polymers can span over eight orders of magnitude upon doping with up to 10% by weight of nanotubes [Zyv]. These polymers are expected to find application in electrostatic painting and EMI shielding.

In the short time since their discovery, CNTs have seen many exciting scientific discoveries and showed much promise in applications.

## Acknowledgments

MPA would like to acknowledge NASA Contract NAS2-03144 to the University Affiliated Research Centre, UC, Santa Cruz. Sandia is a multiprogram laboratory operated by the Sandia Corporation, a Lockheed Martin Company, for the United States Department of Energy under contract DE-AC01-94-AL85000.

## References

[Ade00] Adessi Ch and Devel M 2000 *Phys. Rev.* B **62** R13314
[Ago00] Ago H *et al* 1999 *J. Phys. Chem.* B **103** 8116
Suzuki S, Bower C and Watanabe Y 2000 *Appl. Phys. Lett.* **76** 4007

[Ana98] Anantram M P and Govindan T R 1998 *Phys. Rev.* B **58** 4882
[Ana00] Anantram M P 2000 *Phys. Rev.* B **62** 4837
[Ana00b] Anantram M P, Datta S and Xue Y 2000 *Phys. Rev.* B **61** 14219
[Ana01] Anantram M P 2001 *Appl. Phys. Lett.* **78** 2055
[And98] Ando T and Nakanishi T 1998 *J. Phys. Soc. Japan.* **67** 1704
[And00] Andriotis A N, Menon M and Froudakis G E 2000 *Appl. Phys. Lett.* **76** 3890
[Ape02] Appenzeller J, Knoch J, Derycke V, Martel R, Wind S and Avouris Ph 2002 *Phys. Rev. Lett.* **89** 126801
[App04] Appenzeller J 2004 *Phys. Rev. Lett.* **92** 048301
[Bab03] Babic B, Furer J, Sahoo S, Farhangfar Sh and Schonenberger C 2003 *Nano Lett.* **2** 1577
[Bac01] Bachtold A, Hadley P, Nakanishi T and Dekker C 2001 *Science* **294** 1317
[Bes03] Besteman K, Lee J-O, Wiertz F G M, Heering H A and Dekker C 2003 *Nano Lett.* **3** 727
[Bau99] Baughman R H *et al* 1999 *Science* **284** 1340
[Bla94] Blasé X, Benedict L X, Shirley E L and Louie S G 1994 *Phys. Rev. Lett.* **72** 1878
[Boc99a] Bockrath M, Cobden D H, Lu J, Rinzler A G, Smalley R E, Balents L and McEuen P L 1999 *Nature* **397** 598
[Boc99] Bockrath M W 1999 *PhD Thesis* Univeristy of California, Berkeley
[Bon99] Bonard J-M, Salvetat J-P, Stöckli T, Forró L and Châtelain A 1999 *Appl. Phys. A: Mater. Sci. Process.* **69** 245
[Bon02] Bonard J-M , Dean K A, Coll B F and Klinke C 2002 *Phys. Rev. Lett.* **89** 197602
[Bou04] Bourlon B, Glattli D C, Plaçais B, Berroir J M, Miko C, Forró L and Bachtold A 2004 *Phys. Rev. Lett.* **92** 026804
[Bur02] Burke P J 2002 *IEEE Trans. Nanotechnol.* **1** 129
[Cab03] Cabria I, Mintmire J W and White C T 2003 *Phys. Rev.* B **67** 121406
[Car97] Carroll D L, Redlich P, Ajayan P M, Charlier J C, Blase X, De Vita A and Car R 1997 *Phys. Rev. Lett.* **78** 2811
[Che95] Chernozatonskii L A, Gulyaev Yu V, Kosakovskaja Z Ja, Sinitsyn N I, Torgashov G V, Zakharchenko Yu F, Fedorov E A and Val'chuk V P 1995 *Chem. Phys. Lett.* **233** 63
[Cho99] Choi H J, Ihm J, Yoon Y-G and Louie S G 1999 *Phys. Rev.* B **60** R14009
[Cho00] Choi H J, Ihm J, Louie S G and Cohen M L 2000 *Phys. Rev. Lett.* **84** 2917
[Cho99a] Choi W B *et al* 1999 *Appl. Phys. Lett.* **75** 3129
[Col01] Collins P G, Hersam M, Arnold M, Martel R and Avouris Ph 2001 *Phys. Rev. Lett.* **86** 3128–31
[Cro04] Croci M, Arfaoui I, Stöckli T, Chatelain A and Bonard J-M 2004 *Microelectron. J.* **35** 329
[Dea00] Dean K A and Chalamala B R 2000 *Appl. Phys. Lett.* **76** 375
[Der01] Derycke V, Martel R, Appenzeller J and Avouris Ph 2001 *Nano Lett.* **292** 453
[Fra98] Frank S, Poncharal P, Wang Z L and de Heer W A 1998 *Science* **280** 1744
Poncharal P, Berger C, Yi Y, Wang Z L and de Heer W A 2002 *J. Phys. Chem.* B **106** 12104
[Fre03] Freitag M, Martin Y, Misewich J A, Martel R and Avouris Ph 2003 *Nano Lett.* **3** 1067
[Fre04] Freitag M, Perebeinos V, Chen J, Stein A, Tsang J C, Misewich J A, Martel R and Avouris Ph 2004 *Nano Lett.* **4** 1063
[Fre04a] Freitag M, Chen J, Tersoff J, Tsang J C, Fu Q, Liu J and Avouris Ph 2004 *Phys. Rev. Lett.* **93** 076803
[Fuh00] Fuhrer M S *et al* 2000 *Science* **288** 494
[Gar03] Gartstein Yu N, Zakhidov A A and Baughman R H 2003 *Phys. Rev.* B **68** 115415
[Gom04] Gómez-Navarro C, de Pablo P J and Gómez-Herrero J 2004 *Adv. Mater.* **16** 549
[Gra01] Graugnard E, dePablo P J, Walsh B, Ghosh A W, Datta S and Reifenberger R 2001 *Phys. Rev.* B **64** 125407
[Gom05] Gomez-Navarro C, de Pablo P J, Gomez-Herrero J, Biel B, Garcia-Vidal F J, Rubio A and Flores F 2005 *Nature Mater.* **4** 534
[Gul02] Gülseren O, Yildirim T, Ciraci S, and Kılıç Ç 2002 *Phys. Rev.* B **65** 155410
[Han98] Han J, Anantram M P, Jaffe R L, Kong J and Dai H 1998 *Phys. Rev.* B **57** 14983–89
[Hee95] de Heer W A, Chatelain A and Ugarte D 1995 *Science* **270** 1179
[Hey97] Heyd R, Charlier A and McRae E 1997 *Phys. Rev.* B **55** 6820
[Jav03] Javey A *et al* 2003 *Nature* **424** 654
[Jon04] de Jonge N, Allioux M, Doytcheva M, Kaiser M, Teo K B K, Lacerda R G and Milne W I 2004 *Appl. Phys. Lett.* **85** 1607
[Kil00] Kılıç Ç, Ciraci S, Gülseren O and Yildirim T 2000 *Phys. Rev.* B **62** 16345
[Kle01] Alex Kleiner and Sebastian Eggert 2001 *Phys. Rev.* B **63** 73408
[Kon00] Kong J, Franklin N R, Zhou C, Chapline M G, Peng S, Cho K and Dai H 2000 *Science* **287** 622
[Kon01] Kong J, Yenilmez E, Tombler T W, Kim W, Dai H, Laughlin R B, Liu L, Jayanthi C S and Wu S Y 2001 *Phys. Rev. Lett.* **87** 106801

[Kre02] Kreupl F, Graham A P, Duesberg G S, Steinhogl W, Liebau M, Unger E and Honlein W 2002 *Microelectron. Eng.* **64** 399
[Lee04] Lee J U, Gipp P P and Heller C M 2004 *Appl. Phys. Lett.* **85** 145
[Leo99] Léonard F and Tersoff J 1999 *Phys. Rev. Lett.* **83** 5174
[Leo00a] Léonard F and Tersoff J 2000 *Phys. Rev. Lett.* **84** 4693
[Leo00] Léonard F and Tersoff J 2000 *Phys. Rev. Lett.* **85** 4767
[Leo02] Léonard F and Tersoff J 2002 *Phys. Rev. Lett.* **88** 258302
[Leo05] Leonard F, Jones F E, Talin A A and Dentinger P M 2005 *Appl. Phys. Lett.* **86** 093112
[Li04] Li J 2004 *Chemical and Physical Sensors in Carbon Nanotubes: Science and Applications* ed M Meyyappan (Boca Raton, FL: CRC Press)
[Li04a] Li J 2004 *Application: Biosensors in Carbon Nanotubes: Science and Applications* ed M Meyyappan (Boca Raton FL: CRC Press)
[Lia04] Liang Y X, Li Q H and Wang T H 2004 *Appl. Phys. Lett.* **84** 3379
[Liu03] Liu Y 2003 *Phys. Rev.* B **68** 193409
[Liu00] Liu L, Jayanthi C S, Tang M, Wu S Y, Tombler T W, Zhou C, Alexseyev L, Kong J and Dai H 2000 *Phys. Rev. Lett.* **84** 4950
[Lov00] Lovall D, Buss M, Graugnard E, Andres R P and Reifenberger R 2000 *Phys. Rev.* B **61** 5683
[Lu03] Lu J-Q, Wu J, Duan W, Liu F, Zhu B-F and Gu B-L 2003 *Phys. Rev. Lett.* **90** 156601
[Mai02] Maiti A, Svizhenko A and Anantram M P 2002 *Phys. Rev. Lett.* **88** 126805
[Mar98] Martel R, Schmidt T, Shea H R, Hertel T and Avouris Ph 1998 *Appl. Phys. Lett.* **73** 2447
[Meh05] Mehrez H, Svizhenko A, Anantram M P, Elstner M and Frauenheim T 2005 *Phys. Rev.* B **71** 155421
[Min98] Mintmire J W and White C T 1998 *Phys. Rev. Lett.* **81** 2506–9
[Min03] Minot E D, Yaish Y Y, Sazonova V, Park J-Y, Brink M and McEuen P L 2003 *Phys. Rev. Lett.* **90** 156401
[Mis03] Misewich J A, Martel R, Avouris Ph, Tsang J C, Heinze S and Tersoff J 2003 *Science* **300** 783
[Nar99] Nardelli M B and Bernnholc J 1999 *Phys. Rev.* B **60** R16338–41
[Ngo04] Ngo Q, Petranovic D, Krishnan S, Cassell A M, Ye Q, Li J, Meyyappan M and Yang C Y 2004 *IEEE Trans. Nanotechnol.* **3** 311
[Nil00] Nilsson L, Groening O, Emmenegger C, Kuettel O, Schaller E, Schlapbach L, Kind H, Bonard J-M and Kern K 2000 *Appl. Phys. Lett.* **76** 2071
[Pal03] Palacios J J, Pérez-Jiménez A J, Louis E, SanFabián E and Vergés J A 2003 *Phys. Rev. Lett.* **90** 106801
[Par99] Park C J, Kim Y H and Chang K J 1999 *Phys. Rev.* B **60** 10656
[Par04] Park J, Rosenblatt S, Yaish Y, Sazonova V, Ustunel H, Braig S, Arias T A, Brouwer P W and McEuen P L 2004 *Nano Lett.* **4** 517
[Pau99] Paulson S, Falvo M R, Snider N, Helser A, Hudson T, Seeger A, Taylor R M, Superfine R and Washburn S 1999 *Appl. Phys. Lett.* **75** 2936
[Pau00] Paulson S, Helser A, Buongiorno Nardelli M, Taylor II R M, Falvo M, Superfine R and Washburn S 2000 Tunable resistance of a carbon nanotube–graphite interface *Science* **290** 1742
[Pon99] Poncharal P, Wang Z L, Ugarte D and de Heer W A 1999 *Science* **283** 1513
[Pur02] Purcell S T, Vincent P, Journet C and Binh V T 2002 *Phys. Rev. Lett.* **89** 276103
[Rin95] Rinzler A G, Hafner J H, Nikolaev P, Lou L, Kim S G, Tomanek D, Nordlander P, Colbert D T and Smalley R E 1995 *Science* **290** 1179
[Roc99] Rochefort A, Avouris P, Lesage F and Salahub D 1999 *Phys. Rev.* B **60** 13824
[Rol 00] Roland C, Nardelli M B, Wang J and Guo H 2000 *Phys. Rev. Lett.* **84** 2921
[Rue00] Rueckes T, Kim K, Joselevich E, Tseng G Y, Cheung C-L and Lieber C M 2000 *Science* **289** 94
[Sal05] Salahuddin S, Lundstrom M and Datta S 2005 *IEEE Trans. Electron. Devices* **52** 1734
[San00] Sanvito S, Kwon Y K, Tomanek D and Lambert C J 2000 *Phys. Rev. Lett.* **84** 1974
[Sar04] Sarrazin P, Blake D, Delzeit L, Meyyappan M, Boyer B, Snyder S and Espinosa B 2004 *Adv. X-Ray Anal.* **46** 232
[Sar05] Sarrazin P, Blake D, Feldman S, Chipera S, Vaniman D and Bish D 2005 *Adv. X-Ray Anal.* **48** 194
[Saz04] Sazonova V, Yaish Y, Ustunel H, Roundy D, Arias T A and McEuen P L 2004 *Nature* **431** 284
[Saz04a] http://www.news.cornell.edu/releases/Sept04/McEuen.nanotube.ws.html
[Ste04] Stewart D A and Léonard F 2004 *Phys. Rev. Lett.* **93** 107401
[Sti05] Stix G 2005 Nanotubes in the clean room *Scientific American* February, p 82
[Sug01] Sugie H, Tanemura M, Filip V, Iwat K, Takahashi K and Okuyama F 2001 *Appl. Phys. Lett.* **78** 2578
[Svi05] Svizhenko A and Anantram M P 2005 *Phys. Rev.* B **72** 085430
[Sze81] Sze S M 1981 *Physics of Semiconductor Devices* (New York: Wiley)
[Tal04] Talin A A *et al* 2006 *J. Electron. Mater.* at press
[Tan98] Tans S J, Verschueren A R M and Dekker C 1998 *Nature* **393** 49

[Tar01] Tarkiainen R, Ahlskog M, Penttilä J, Roschier L, Hakonen, Paalanen M and Sonin E 2001 *Phys. Rev.* B **64** 195412
[Ter94] Tersoff J and Ruoff R S 1994 *Phys. Rev. Lett.* 73 676
[The96] Thess A *et al* 1996 *Science* **273** 483
[Tom00] Tombler T W, Zhou C, Alexseyev L, Kong J, Dai H, Liu L, Jayanthi C S, Tang M and Wu S-Y 2000 *Nature (London)* **405** 769
[Vit99] De Vita A, Charlier J C, Blase X and Car R 1999 *Appl. Phys. A: Solids Surf.* **68** 283
[Wan98] Wang Q H, Setlur A A, Lauerhaas J M, Dai J Y, Seelig E W and Chang R P H 1998 *Appl. Phys. Lett.* **72** 2912
[Wei01] Wei B Q, Vajtai R and Ajayan P M 2001 *Appl. Phys. Lett.* **79** 1172
[Whi93] White C T, Robertson D H and Mintmire J W 1993 *Phys. Rev.* B **47** 5485
[Whi98] White C T and Todorov T N 1998 *Nature* **393** 240
[Whi05] White C T and Mintmire J W 2005 *J. Phys. Chem.* B **109** 52
[Yai04] Yaish Y *et al* 2004 *Phys. Rev. Lett.* **92** 046401
[Yam04] Yamada T 2004 *Nanoelectronics Applications* ed M Meyyappan (Boca Raton, FL: CRC Press)
[Yan99] Yang L, Anantram M P, Han J and Lu J P 1999 *Phys. Rev.* B **60** 13874
[Yan00] Yang L and Han J 2000 *Phys. Rev. Lett.* **85** 154
[Yan02] Yang C K, Zhao J and Lu J P 2002 *Phys. Rev.* B **66** 041403(R)
[Yao99] Yao Z, Postma H W Ch, Balents L and Dekker C 1999 *Nature* **402** 273
[Yao00] Yao Z, Kane C L and Dekker C 2000 *Phys. Rev. Lett.* **84** 2941
[Yoo02] Young-Gui Yoon, Paul Delaney and Louie S G 2002 *Phys. Rev.* B **66** 073407
[Yu05] Yu Z and Burke P J 2005 *Nano Lett.* **5** 1403
[Yue02] Yue G Z, Qiu Q, Gao B, Cheng Y, Zhang J, Shimoda H, Chang S, Lu J P and Zhou O 2002 *Appl. Phys. Lett.* **81** 355
[Zha99] Zhang Y, Ichihashi T, Landree E, Nihey F and Iijima S 1999 *Science* **285** 1719
[Zha05] Zhang J, Yang G, Cheng Y, Gao B, Qiu Q, Lee Y Z, Lu J P and Zhou O 2005 *Appl. Phys. Lett.* **86** 184104
[Zho00] Zhou C, Kong J, Yenilmez E and Dai H 2000 *Science* **290** 1552
[Zyv] Rutkofsky M, Banash M, Rajagopal R and Chen J, Using a Carbon nanotube additive to make electrically conductive commercial polymer composites http://www.zyvex.com/Documents/9709.PDF